การศึกษาด้วยพลศาสตร์ของไหลเชิงคำนวณในด้านอิทธิพลของการพ่นเป็นจังหวะที่มีต่อการสังเคราะห์สังกะสีออกไซด์ด้วยกระบวนการออกซิเดชันที่ใช้ความร้อน

นายเอกราช บำรุงไทยชัยชาญ

วิทยานิพนธ์นี้เป็นส่วนหนึ่งของการศึกษาตามหลักสูตรปริญญาวิศวกรรมศาสตรมหาบัณฑิต
สาขาวิชาวิศวกรรมเคมี ภาควิชาวิศวกรรมเคมี
คณะวิศวกรรมศาสตร์ จุฬาลงกรณ์มหาวิทยาลัย
ปีการศึกษา 2555

COMPUTATIONAL FLUID DYNAMICS STUDY ON EFFECT OF PULSE INJECTION ON ZINC OXIDE SYNTHESIS BY THERMAL OXIDATION

Mr. Eakarach Bumrungthaichaichan

A Thesis Submitted in Partial Fulfillment of the Requirements
for the Degree of Master of Engineering Program in Chemical Engineering
Department of Chemical Engineering
Faculty of Engineering
Chulalongkorn University
Academic Year 2012

Thesis Title	COMPUTATIONAL FLUID DYNAMICS STUDY ON EFFECT OF PULSE INJECTION ON ZINC OXIDE SYNTHESIS BY THERMAL OXIDATION
By	Mr. Eakarach Bumrungthaichaichan
Field of Study	Chemical Engineering
Thesis Advisor	Associate Professor Tawatchai Charinpanitkul, D.Eng.
Thesis Co-advisor	Pimporn Ponpesh, Ph.D.

Accepted by the Faculty of Engineering, Chulalongkorn University in Partial Fulfillment of the Requirements for the Master's Degree

.....Dean of the Faculty of Engineering
(Associate Professor Boonsom Lerdhirunwong, Dr.Ing.)

THESIS COMMITTEE

.....Chairman
(Assistant Professor Varong Pavarajarn, Ph.D.)

.....Thesis Advisor
(Associate Professor Tawatchai Charinpanitkul, D.Eng.)

.....Thesis Co-advisor
(Pimporn Ponpesh, Ph.D.)

.....Examiner
(Assistant Professor Apinan Soottitantawat, D.Eng.)

.....External Examiner
(Santi Wattananusorn, Dr.Ing.)

เอกราช บำรุงไทยชัยชาญ : การศึกษาด้วยพลศาสตร์ของไหลเชิงคำนวณในด้านอิทธิพลของการพ่นเป็นจังหวะที่มีต่อการสังเคราะห์สังกะสีออกไซด์ด้วยกระบวนการออกซิเดชันที่ใช้ความร้อน (COMPUTATIONAL FLUID DYNAMICS STUDY ON EFFECT OF PULSE INJECTION ON ZINC OXIDE SYNTHESIS BY THERMAL OXIDATION) อ. ที่ปรึกษาวิทยานิพนธ์หลัก: รศ.ดร. ธวัชชัย ชรินพาณิชกุล, อ. ที่ปรึกษาวิทยานิพนธ์ร่วม: ดร. พิมพ์พร พลเพชร, 73 หน้า.

งานวิจัยนี้ ศึกษาอิทธิพลของการพ่นเป็นจังหวะในกระบวนการสังเคราะห์สังกะสีออกไซด์ด้วยกระบวนการออกซิเดชันที่ใช้ความร้อนด้วยพลศาสตร์ของไหลเชิงคำนวณ ผลได้ของสังกะสีออกไซด์ที่ตำแหน่งการพ่นเป็นจังหวะที่แตกต่างกันจะถูกคำนวณด้วยโปรแกรม FLUENT แล้วนำมาเปรียบเทียบกับผลการทดลอง เพื่อยืนยันความถูกต้องของแบบจำลองที่สร้างขึ้น พลศาสตร์ของไหลเชิงคำนวณได้ทำนายผลกระทบของตำแหน่งการพ่นเป็นจังหวะ ผลกระทบของลักษณะการพ่น และผลกระทบของตำแหน่งการปล่อยอากาศที่มีต่อผลได้ของสังกะสีออกไซด์ จากผลการจำลองพบว่าปริมาณของสังกะสีออกไซด์ที่มากที่สุดจะเกิดขึ้นที่ตำแหน่งการพ่นเป็นจังหวะเท่ากับตำแหน่งที่เกิดความเร็วเหนี่ยวนำสูงสุด (Entrainment velocity) สาเหตุที่ทำให้เกิดปริมาณของสังกะสีออกไซด์สูงสุดเนื่องจากตำแหน่งนี้จะเกิดการเหนี่ยวนำให้ไอของสังกะสีเข้าไปทำปฏิกิริยากับอากาศซึ่งเป็นผลมาจากเจ็ทของอากาศและความปั่นป่วนที่เกิดจากการพ่นเป็นจังหวะ ผลกระทบของลักษณะการพ่นพบว่าการพ่นแบบต่อเนื่องจะทำให้ปริมาณของสังกะสีออกไซด์มากกว่าการพ่นเป็นจังหวะ ซึ่งเป็นผลมาจากพลังงานจลน์ของความปั่นป่วน (Turbulent kinetic energy) ที่ตำแหน่งการพ่นและระยะเวลาของการพ่นแบบต่อเนื่องมีค่ามากกว่าการพ่นเป็นจังหวะ ผลกระทบของตำแหน่งการปล่อยอากาศพบว่า การปล่อยอากาศในลักษณะตามกระแส (Co-current) จะมีผลได้ของสังกะสีออกไซด์สูงกว่าการปล่อยอากาศแบบขวางกระแส (Cross current)

ภาควิชา วิศวกรรมเคมี ลายมือชื่อนิสิต .....

สาขาวิชา วิศวกรรมเคมี ลายมือชื่อ อ.ที่ปรึกษาวิทยานิพนธ์หลัก .....

ปีการศึกษา 2555 ลายมือชื่อ อ.ที่ปรึกษาวิทยานิพนธ์ร่วม .....

5370531021: MAJOR CHEMICAL ENGINEERING
KEYWORDS : COMPUTATIONAL FLUID DYNAMICS/
ZINC OXIDE/THERMAL OXIDATION/PULSE INJECTION

EAKARACH BUMRUNGTHAICHAICHAN: COMPUTATIONAL FLUID DYNAMICS STUDY ON EFFECT OF PULSE INJECTION ON ZINC OXIDE SYNTHESIS BY THERMAL OXIDATION. ADVISOR: ASSOC. PROF. TAWATCHAI CHARINPANITKUL, D.Eng., CO-ADVISOR: PIMPORN PONPESH, Ph.D., 73 pp.

In this work, The effect of pulse injection on zinc oxide synthesis by thermal oxidation using Computational Fluid Dynamics (CFD) were studied. The yields of zinc oxide for different pulse injection positions were simulated using FLUENT® software. The simulation results were validated by comparing with published experimental data. The effect of pulse injection, including pulse injection position, pulse characteristic, and air feed position on yields of zinc oxide were predicted. The simulated results showed that the maximum yield of zinc oxide occurred at the pulse injection position which maximum entrainment velocity were observed. The maximum yield of zinc oxide occurred at this position because of the maximum entrainment velocity due to air jet and the turbulent mixing due to nitrogen pulse injection. The yields of continuous injection were greater than pulse injection because the turbulent kinetic energy at injection position and injection period of continuous injection were higher than pulse injection. The simulated results of air feed position effect revealed that the yields of zinc oxide for co-current were slightly greater than cross current.

Department : Chemical Engineering	Student's Signature .....
Field of Study : Chemical Engineering	Advisor's Signature .....
Academic Year : 2012	Co-advisor's Signature .....

ACKNOWLEDGEMENTS

I am very thankful to my thesis advisor and co-advisor, Assoc Prof. Tawatchai Charinpanitkul and Dr. Pimporn Ponpesh, Department of Chemical Engineering, Chulalongkorn University, for their introducing me to this interesting project, and for their helpful and deep discussion and encouraging guidance throughout the course of this work. Furthermore, I am also thankful to Asst. Prof. Varong Pavarajarn, Dr. Santi Wattananusorn, and Asst. Prof. Apinan Soottitantawat for their comments and participation as my thesis committee.

The FLUENT® software has been supported by Computer Services Center, King Mongkut's Institute of Technology Ladkrabang (KMITL). This work was also partially by Centenary Fund of Chulalongkorn University for the partial financial support to this work.

Furthermore, I would like to thank all members of Center of Excellence in Particle Technology for their help, suggestion and warm collaborations.

Finally, I would like to express my cordial and deep thanks to my family for their love and encouragement.

CONTENTS

Page

CHAPTER **Page**

CHAPTER **Page**

CHAPTER **Page**

LIST OF TABLES

LIST OF FIGURES

Figure **Page**

Figure **Page**

Figure **Page**

LIST OF ABBREVIATIONS

ALPHABETICAL SYMBOLS

$D_{i,m}$	Mass diffusion coefficient for species i in the mixture
$D_{T,i}$	Thermal (Soret) diffusion coefficient
E	Total energy
G_b	The generation of turbulent due to buoyancy
G_k	The production of turbulent due to buoyancy
g	Gravitational force
$\overrightarrow{J_i}$	Diffusion flux of species i
k	Turbulent kinetic energy
k	Thermal conductivity
k_{eff}	Effective thermal conductivity
k_0	Reaction rate constant
M_t	Turbulent Mach number
Pr_t	Turbulent Prandtl number
p	pressure
$\bar{p}$	Mean value of pressure
p'	Fluctuating component of pressure
R	Universal gas constant
R_i	Net rate of production of species i by chemical reaction
S_E	Total energy source term

S_h	Energy source term
S_i	Species source term
S_k	Turbulent kinetic energy source term
S_{Mx}, S_{Mx}, S_{Mx}	Momentum source term in x, y, z directions
S_ε	Dissipation rate of turbulent kinetic energy source term
Sc_t	Turbulent Schmidt number
t	Time
T	Temperature
$\mathbf{U}$	Velocity vector
$\mathbf{U}'$	Fluctuating of velocity vector
$\overline{\mathbf{U}}$	Mean value of velocity vector
u, v, w	Velocity components in x, y, z directions
u', v', w'	Fluctuating components of velocity in x, y, z directions
$\bar{u}$, $\bar{v}$, $\bar{w}$	Mean velocity components in x, y, z directions
$\overline{u_i}$, $\overline{u_j}$, $\overline{u_k}$	Mean value of velocity components in i, j, k directions
$\overline{u_i'}$, $\overline{u_j'}$	Mean value of fluctuating velocity components in i, j directions
x, y, z	Rectangular coordinates
Y_i	Mass fraction of species i
Y_M	Dilatation dissipation term

GREEK SYMBOLS

β	Thermal expansion coefficient
ε	Dissipation rate of turbulent kinetic energy
μ	Viscosity
μ_t	Turbulent viscosity
μ_{eff}	Effective viscosity
ρ	Fluid density
τ_{xx}, τ_{yy}, τ_{zz}	Normal stresses on y-z, x-z, x-y planes
τ_{xy}, τ_{xz}, τ_{yz}	Shear stresses on x-z, y-z, x-y planes
$\bar{\tau}_{ij}^{(t)}$	Turbulent shear stress

CHAPTER I

INTRODUCTION

1.1 Background and Motivation

Since 1960s, the aerospace industry has integrated Computational Fluid Dynamics (CFD) techniques into design, R&D, and manufacturing of aircraft and jet engines. Nowadays, this method have been applied to analyze the various fluid flow problems and becomes an important engineering tool because CFD can produce extremely large volumes of results at virtually low expense to perform parametric studies [1]. CFD is a branch of fluid mechanics that uses numerical method and algorithm to solve and analyze momentum, heat, and mass transfer in various systems. Phenomena of fluid flow are usually explained by three fundamental physical laws, including the conservation of mass, the Newton's second law of motion, and the first law of thermodynamics. CFD is very useful and spans a wide range of application areas. For example, fluid flow pattern in cyclone separator [2], membrane separation [3], reactor optimization [4], heat transfer in packed bed column [5], etc.

Zinc oxide is an inorganic compound with the formula ZnO appearing as a white powder. Zinc oxide is known as a II-VI semiconductor with useful electronic properties, which are wide band gap energy (3.37 eV) and high exciton binding energy (60 meV). Because of its electronic properties, zinc oxide is an excellent candidate for the fabrication of nanoelectronic and photonic devices. Zinc oxide has various nanostructures, such as nanorods [6], nanoneedle structures [7], comb structures [8], tetrapods [9], which depend on different synthesizing routes and conditions, such as Metal Oxide Chemical Vapor Deposition (MOCVD) [10], hydrothermal treatment [11], thermal oxidation [12-14]. Among these method, the thermal oxidation of zinc vapor provides a highly efficient and simple protocol as it requires only mixing the two feeds of zinc vapor and oxygen in a closed system to allow the oxidation of zinc at a high temperature.

Regarding to the benefits of CFD and requirement of controlled synthesis of zinc oxide, many researchers use CFD techniques combine with experimental results to describe the phenomena of zinc oxide formation [4, 15]. Those important parameters would be pressure profiles, velocity profiles, temperature profiles, mass fraction of chemical components, etc. Though, there are some previous works related to numerical investigation of zinc oxide synthesis, clear understanding on formation of zinc oxide in the thermal oxidation process is still a challenging issue worthwhile for farther examination.

The objective of this research is to investigate the effects of pulse injection on yield of zinc oxide by using FLUENT® commercial CFD code. The k-epsilon turbulent model and species transport equations with finite reaction rate are used to compute fluid motions and yield of zinc oxide.

1.2 Objectives of the Research

The objective of this research is to investigate the effect of pulsed injection on zinc oxide synthesis by thermal oxidation which is modified with pulse injection by using FLUENT®.

1.3 Scope of the Research

1.3.1 Validation of simulation models ; Comparison between simulation results and experimental results

1.3.2 Employ CFD technique using FLUENT® to study zinc oxide synthesis by thermal oxidation. The following synthesis parameters are investigated for their effects on yields of zinc oxide,

- Effect of pulse injection position, including 0.5, 2.5, and 5.5 cm from outlet of air feed tube
- Effect of pulse characteristic, including pulse and continuous
- Effect of air feed position, including co-current and cross current

1.4 Procedure of the Research

- Conduct literature survey and review
- Model setup (e.g. Solid modeling, grid generation, etc.)
- Solve problems by using FLUENT® and investigate grid independent solutions
- Compare simulation results with experiment data which reported in other previous works
- Simulation of synthesis parameters which effect on yield of zinc oxide
- Making discussion and conclusion of simulation results
- Writing thesis and preparation of draft manuscript for journal publication

1.5 Expected Benefit

- Obtain knowledge of zinc oxide synthesis by pulse thermal oxidation using FLUENT®

CHAPTER II

THEORY AND LITERATURE REVIEW

2.1 Computational Fluid Dynamics (CFD)

Computational fluid dynamics or CFD is a branch of fluid mechanics that uses numerical technique and algorithm to solve and analyze various flow problems. CFD becomes an important engineering tool because it can provide clear insight into many fluid flow phenomena and produce extremely large volumes of results with inexpensive operating cost. CFD is very powerful and spans a wide range of engineering application areas e.g., aerodynamics of aircraft and vehicles, hydrodynamics of ships, mixing and separation in chemical processes, etc.

2.1.1 CFD processing

Generally, CFD program contains three main processes, including pre-processor, solver, and post-processor [1].

pre-processor

This step consists of the input of flow problem to a CFD program, such as definition of the computational domain, grid generation, selection of the physical and chemical phenomena, definition of material properties, etc.

solver

There are three distinct streams of numerical solution technique, including finite difference method, finite element method, and finite volume methods. Generally, the solver performs the following steps,

- Approximation of unknown flow variables by simple function.
- Transform the PDEs into algebraic equation. This step is called discretisation.

- Solution of the algebraic equations.

post-processor

Post-processor contains versatile data visualization tools, such as geometry and grid display, vector plot, line and shaded contour plots, etc

CFD processing can be summarized as a diagram, which shown in Figure 2.1.

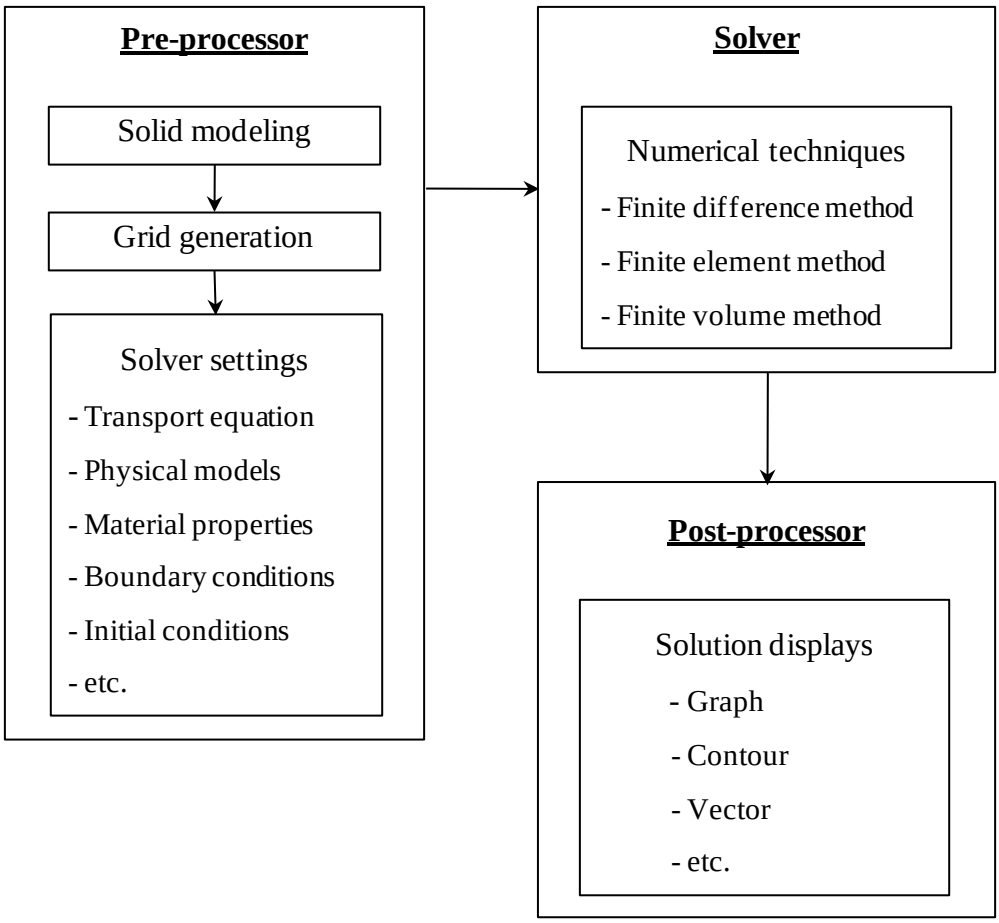

Figure 2.1 CFD processing diagram

2.1.2 Finite volume method

Finite volume method is numerical solution technique. This method was originally developed as a special finite difference formulation. Finite volume method consists of the following steps,

- Integration of fluid flow governing equations over control volume.
- Discretisation involves the substitution of a variety of finite-difference-type approximations in the integrated equation, including convection term, diffusion term and source term. This converts the integral equations into a set of algebraic equations.
- Solution of the algebraic equations by an iterative method.

2.2 Governing equations

The fluid problems are usually governed by three fundamental physical equations, including the conservation of mass, the Newton's second law of motion, and the first law of thermodynamics.

2.2.1 Mass conservation equation

The conservation of mass states that mass may be neither created nor destroyed. The mass conservation equation or continuity equation is given by

$$\frac{\partial \rho}{\partial t} + \frac{\partial}{\partial x}(\rho u) + \frac{\partial}{\partial y}(\rho v) + \frac{\partial}{\partial z}(\rho w) = 0 \tag{1}$$

or

$$\frac{\partial \rho}{\partial t} + \nabla \cdot (\rho \mathbf{U}) = 0 \tag{2}$$

where $\mathbf{U}$ is the velocity vector in cartesian coordinate and given by

$$\mathbf{U} = u\mathbf{i} + v\mathbf{j} + w\mathbf{k}$$

where $\mathbf{i}$, $\mathbf{j}$, and $\mathbf{k}$ are the unit vectors along x, y, and z axes, respectively.

2.2.2 Momentum equations

The Newton's second law of motion states that the time rate of change of momentum of a system is equal to the net force acting on the system and takes place in the direction of the net force. The three momentum conservation equations are given by

x-component:

$$\rho\frac{Du}{Dt}=\frac{\partial}{\partial t}(\rho u)+\nabla\cdot(\rho u\mathbf{U})=-\frac{\partial p}{\partial x}+\frac{\partial \tau_{xx}}{\partial x}+\frac{\partial \tau_{yx}}{\partial y}+\frac{\partial \tau_{zx}}{\partial z}+S_{Mx} \qquad (3)$$

y-component:

$$\rho\frac{Dv}{Dt}=\frac{\partial}{\partial t}(\rho v)+\nabla\cdot(\rho v\mathbf{U})=-\frac{\partial p}{\partial y}+\frac{\partial \tau_{xy}}{\partial x}+\frac{\partial \tau_{yy}}{\partial y}+\frac{\partial \tau_{zy}}{\partial z}+S_{My} \qquad (4)$$

z-component:

$$\rho\frac{Dw}{Dt}=\frac{\partial}{\partial t}(\rho w)+\nabla\cdot(\rho w\mathbf{U})=-\frac{\partial p}{\partial z}+\frac{\partial \tau_{xz}}{\partial x}+\frac{\partial \tau_{yz}}{\partial y}+\frac{\partial \tau_{zz}}{\partial z}+S_{Mz} \qquad (5)$$

2.2.3 Energy equation

The first law of thermodynamics states that if a system is carried through a cycle, the total heat added to the system from its surroundings is proportional to the work done by the system on its surroundings. The energy equation in term of total energy (E) is given by

$$\begin{aligned}\rho\frac{DE}{Dt}=&-\frac{\partial(up)}{\partial x}-\frac{\partial(vp)}{\partial y}-\frac{\partial(wp)}{\partial z}+\frac{\partial}{\partial x}\left(k\frac{\partial T}{\partial x}\right)+\frac{\partial}{\partial y}\left(k\frac{\partial T}{\partial y}\right)+\frac{\partial}{\partial z}\left(k\frac{\partial T}{\partial z}\right)\\&+\frac{\partial(u\tau_{xx})}{\partial x}+\frac{\partial(u\tau_{yx})}{\partial y}+\frac{\partial(u\tau_{zx})}{\partial z}+\frac{\partial(v\tau_{xy})}{\partial x}+\frac{\partial(v\tau_{yy})}{\partial y}+\frac{\partial(v\tau_{zy})}{\partial z}\\&+\frac{\partial(w\tau_{xz})}{\partial x}+\frac{\partial(w\tau_{yz})}{\partial y}+\frac{\partial(w\tau_{zz})}{\partial z}+S_E \qquad (6)\end{aligned}$$

Equations (1)-(6) are called the compressible Navier-Stokes equations.

2.3 Turbulence and k-epsilon turbulence model

Fluid flow pattern, including laminar, transition, and turbulent can be identified by Reynolds number (Re). The Reynolds number can be defined as the relative importance of inertia forces and viscous forces. In experiments on fluid systems it is

observed that at values below the critical Reynolds number (Re_{crit}), the flow is smooth and adjacent layers of fluid slide past each other in an orderly fashion. This regime is called laminar flow. At values above Re_{crit}, a complicated series of events takes place which eventually leads to a radical change of the flow character. In the final state the flow behavior is random and chaotic even with constant imposed boundary conditions. This regime is called turbulent flow [1, 16].

2.3.1 Characteristics of the turbulent flow

- Highly unsteady: The velocity is a function of time. The typical point velocity measurement might exhibit the form shown in Figure 2.2.

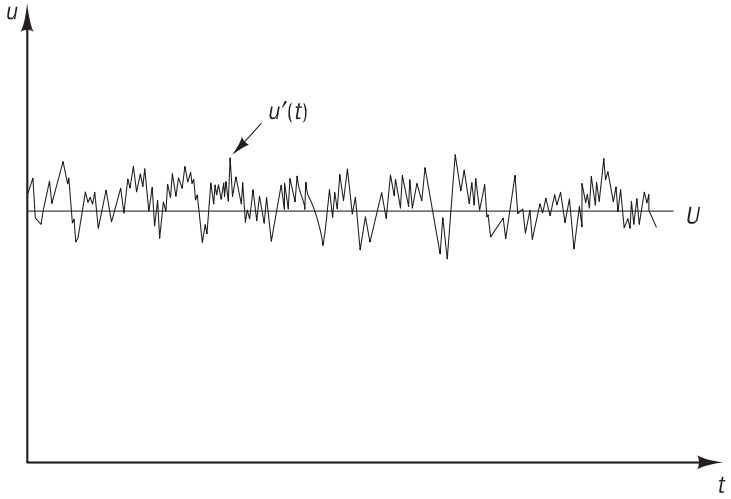

Figure 2.2 Typical point velocity in turbulent flow [1]

- Irregularity: It is another characteristic which makes the deterministic approach to turbulence problems impossible. One should relay on statistical approach.
- Diffusivity: If the flow pattern is random but does not exhibit spreading of velocity fluctuations through the surrounding fluid then the flow is not turbulent. This characteristic of turbulence causes rapid mixing and increased rates of momentum, heat, and mass transfer.
- Three dimensional: Turbulence is three dimensional and rotational.
- Dissipative: The turbulent flows are always dissipative.

- Higher Reynolds number: Turbulence in the fluid flow always occurs at high Reynolds numbers.

2.3.2 Reynolds average Navier-Stokes equations (RANS)

According to irregular characteristic of turbulent flow, the computations based on the complete description of all fluid particles motion are impossible. However, the computations of turbulent flow can be solved by using statistical approach [16]. The instantaneous flow property (φ) is decomposed into its time-averaged ($\overline{\varphi}$) and fluctuating quantities (φ') as shown in equation (7).

$$\varphi(t) = \overline{\varphi} + \varphi'(t) \tag{7}$$

This process is called Reynolds decomposition, which first proposed by Osborne Reynolds. The definition of time-average of flow property (φ) and time-average of fluctuation property (φ') are given by

$$\overline{\varphi} = \frac{1}{\Delta t}\int_0^{\Delta t} \varphi(t)dt \tag{8}$$

$$\overline{\varphi'} = \frac{1}{\Delta t}\int_0^{\Delta t} \varphi'(t)dt \equiv 0 \tag{9}$$

Regarding to Reynolds decomposition, pressure, velocity vector, and three velocity components, including x-, y-, and z-component can be expressed as

$$p(t) = \overline{p} + p'(t) \tag{10}$$

$$\mathbf{U}(t) = \overline{\mathbf{U}} + \mathbf{U}'(t) \tag{11}$$

$$u(t) = \overline{u} + u'(t) \tag{12}$$

$$v(t) = \overline{v} + v'(t) \tag{13}$$

$$w(t) = \overline{w} + w'(t) \tag{14}$$

The effects of fluctuations on mean flow can be investigated by replace the equations (10)-(14) into governing equations and apply time-average of flow property as shown in equations (8) and (9).

The compressible continuity equation for the mean flow is given by

$$\frac{\partial \rho}{\partial t}+\frac{\partial}{\partial x}\left(\rho \bar{u}\right)+\frac{\partial}{\partial y}\left(\rho \bar{v}\right)+\frac{\partial}{\partial z}\left(\rho \bar{w}\right)=0 \tag{15}$$

or

$$\frac{\partial \rho}{\partial t}+\nabla \cdot \left(\rho \bar{\mathbf{U}}\right)=0 \tag{16}$$

The time-average momentum equations for compressible fluid with constant viscosity are given by

x-component:

$$\begin{aligned}&\frac{\partial}{\partial t}\left(\rho \bar{u}\right)+\frac{\partial}{\partial x}\left(\rho \bar{u}^{2}\right)+\frac{\partial}{\partial y}\left(\rho \bar{u}\bar{v}\right)+\frac{\partial}{\partial z}\left(\rho \bar{u}\bar{w}\right)\\&\quad=-\frac{\partial \bar{p}}{\partial x}+\mu \frac{\partial^{2}\bar{u}}{\partial x^{2}}+\mu \frac{\partial^{2}\bar{u}}{\partial y^{2}}+\mu \frac{\partial^{2}\bar{u}}{\partial z^{2}}\\&\qquad+\left[-\frac{\partial}{\partial x}\left(\rho \overline{\left(u'\right)^{2}}\right)-\frac{\partial}{\partial y}\left(\rho \overline{u'v'}\right)-\frac{\partial}{\partial z}\left(\rho \overline{u'w'}\right)\right]+S_{Mx}\end{aligned} \tag{17}$$

or

$$\begin{aligned}&\frac{\partial}{\partial t}\left(\rho \bar{u}\right)+\nabla \cdot \left(\rho \bar{u}\bar{\mathbf{U}}\right)=-\frac{\partial \bar{p}}{\partial x}+\mu \nabla^{2}\bar{u}\\&\qquad+\left[-\frac{\partial}{\partial x}\left(\rho \overline{\left(u'\right)^{2}}\right)-\frac{\partial}{\partial y}\left(\rho \overline{u'v'}\right)-\frac{\partial}{\partial z}\left(\rho \overline{u'w'}\right)\right]+S_{Mx}\end{aligned} \tag{18}$$

y-component:

$$\begin{aligned}&\frac{\partial}{\partial t}\left(\rho \bar{v}\right)+\frac{\partial}{\partial x}\left(\rho \bar{v}\bar{u}\right)+\frac{\partial}{\partial y}\left(\rho \bar{v}^{2}\right)+\frac{\partial}{\partial z}\left(\rho \bar{v}\bar{w}\right)\\&\quad=-\frac{\partial \bar{p}}{\partial y}+\mu \frac{\partial^{2}\bar{v}}{\partial x^{2}}+\mu \frac{\partial^{2}\bar{v}}{\partial y^{2}}+\mu \frac{\partial^{2}\bar{v}}{\partial z^{2}}\\&\qquad+\left[-\frac{\partial}{\partial x}\left(\rho \overline{u'v'}\right)-\frac{\partial}{\partial y}\left(\rho \overline{\left(v'\right)^{2}}\right)-\frac{\partial}{\partial z}\left(\rho \overline{v'w'}\right)\right]+S_{My}\end{aligned} \tag{19}$$

or
$$\frac{\partial}{\partial t}\left(\rho\bar{v}\right)+\nabla\cdot\left(\rho\bar{v}\overline{\mathbf{U}}\right)=-\frac{\partial\bar{p}}{\partial y}+\mu\nabla^2\bar{v}$$
$$+\left[-\frac{\partial}{\partial x}\left(\rho\overline{u'v'}\right)-\frac{\partial}{\partial y}\left(\rho\overline{(v')^2}\right)-\frac{\partial}{\partial z}\left(\rho\overline{v'w'}\right)\right]+S_{My} \qquad (20)$$

z-component:

$$\frac{\partial}{\partial t}\left(\rho\bar{w}\right)+\frac{\partial}{\partial x}\left(\rho\bar{w}\bar{u}\right)+\frac{\partial}{\partial y}\left(\rho\bar{w}\bar{v}\right)+\frac{\partial}{\partial z}\left(\rho\bar{w}^2\right)$$
$$=-\frac{\partial\bar{p}}{\partial z}+\mu\frac{\partial^2\bar{w}}{\partial x^2}+\mu\frac{\partial^2\bar{w}}{\partial y^2}+\mu\frac{\partial^2\bar{w}}{\partial z^2}$$
$$+\left[-\frac{\partial}{\partial x}\left(\rho\overline{u'w'}\right)-\frac{\partial}{\partial y}\left(\rho\overline{v'w'}\right)-\frac{\partial}{\partial z}\left(\rho\overline{(w')^2}\right)\right]+S_{Mz} \qquad (21)$$

or
$$\frac{\partial}{\partial t}\left(\rho\bar{w}\right)+\nabla\cdot\left(\rho\bar{w}\overline{\mathbf{U}}\right)=-\frac{\partial\bar{p}}{\partial z}+\mu\nabla^2\bar{w}$$
$$+\left[-\frac{\partial}{\partial x}\left(\rho\overline{u'w'}\right)-\frac{\partial}{\partial y}\left(\rho\overline{v'w'}\right)-\frac{\partial}{\partial z}\left(\rho\overline{(w')^2}\right)\right]+S_{Mz} \qquad (22)$$

The equations (17)-(22) are called the Reynolds equation. There are new terms arise in equations (17)-(22), which are associated with turbulent velocity fluctuations. These extra turbulent stresses, which describe the diffusive nature of turbulence [17], are called Reynolds stresses.

For convenience, the new notation of these Reynolds stresses [18] can be expressed as

$$\bar{\tau}_{ij}^{(t)}=-\rho\overline{u_i'u_j'}=\mu_t\left(\frac{\partial\overline{u_i}}{\partial x_j}+\frac{\partial\overline{u_j}}{\partial x_i}\right) \qquad (23)$$

where μ_t is turbulent viscosity or eddy viscosity, which usually depends strongly on position.

The relation in equation (23) was first postulated by Boussinesq in 1877. Thus, equations (18), (20), and (22) become

x-component:

$$\frac{\partial}{\partial t}(\rho\bar{u}) + \nabla\cdot(\rho\bar{u}\bar{\mathbf{U}}) = -\frac{\partial\bar{p}}{\partial x} + \mu_{eff}\nabla^2\bar{u} + S_{Mx} \tag{24}$$

y-component:

$$\frac{\partial}{\partial t}(\rho\bar{v}) + \nabla\cdot(\rho\bar{v}\bar{\mathbf{U}}) = -\frac{\partial\bar{p}}{\partial y} + \mu_{eff}\nabla^2\bar{v} + S_{My} \tag{25}$$

z-component:

$$\frac{\partial}{\partial t}(\rho\bar{w}) + \nabla\cdot(\rho\bar{w}\bar{\mathbf{U}}) = -\frac{\partial\bar{p}}{\partial z} + \mu_{eff}\nabla^2\bar{w} + S_{Mz} \tag{26}$$

where μ_{eff} is the effective viscosity coefficient which is expressed as

$$\mu_{eff} = \mu + \mu_t \tag{27}$$

2.3.3 k-epsilon turbulence model

The k-epsilon model is one of the most common turbulence models which includes two extra transport equations to represent the turbulent properties of the flow. This model was proposed by Launder and Spalding [19]. The first transport equation is transport equation of turbulent kinetic energy (k) and the second one is transport equation of dissipation rate of turbulent kinetic energy (ε). Two transport equations can be shown in equation (28) and (29), respectively.

k-transport equation:

$$\frac{\partial}{\partial t}(\rho k) + \frac{\partial}{\partial x_i}(\rho k\overline{u_i}) = \frac{\partial}{\partial x_j}\left[\left(\mu + \frac{\mu_t}{\sigma_k}\right)\frac{\partial k}{\partial x_j}\right] + G_k + G_b - \rho\varepsilon - Y_M + S_k \tag{28}$$

ε -transport equation:

$$\frac{\partial}{\partial t}(\rho\varepsilon) + \frac{\partial}{\partial x_i}(\rho\varepsilon\overline{u_i}) = \frac{\partial}{\partial x_j}\left[\left(\mu + \frac{\mu_t}{\sigma_\varepsilon}\right)\frac{\partial\varepsilon}{\partial x_j}\right] + C_{1\varepsilon}\frac{\varepsilon}{k}(G_k + C_{3\varepsilon}G_b) - C_{2\varepsilon}\rho\frac{\varepsilon^2}{k} + S_\varepsilon \tag{29}$$

where $\mu_t = \rho C_\mu \frac{k^2}{\varepsilon}$, $G_k = -\rho\overline{u_i' u_j'}\frac{\partial \overline{u_j}}{\partial x_i}$, $G_b = \beta g_i \frac{\mu_t}{\mathrm{Pr}_t}\frac{\partial T}{\partial x_i}$, $Y_M = 2\rho\varepsilon M_t^2$,

$C_{3e} = \tanh\left|\frac{v}{u}\right|$ and the model constants in these equations are shown in Table 2.1.

Table 2.1 Model constant for k-epsilon turbulence model [19]

$C_{1\varepsilon}$	$C_{2\varepsilon}$	C_μ	σ_k	σ_ε
1.44	1.92	0.09	1.0	1.3

2.4 Jet flows

Jet is one of the most common shear flows, which is one fluid stream intruding into another. Common example of intrusion of a fluid into another in chemical engineering is plumes exiting from industrial stacks as shown in Figure 2.3.

Figure 2.3 Plumes exiting from industrial stacks
(http://www.freefoto.com/preview/13-08-1/Chimney-Steam-Smoke)

Jet is one of greater interest to chemical engineer who are concerned with the rate at which two reactants interact with each other [20].

There are many various types of intrusion according to whether they inject momentum, buoyancy, and both momentum and buoyancy in the ambient fluid. The different type of intrusion are shown in Table 2.2

Table 2.2 Types of intrusion of a fluid into another [21]

	Continuous injection	**Intermittent injection**
Momentum only	Jet	Puff
Buoyancy only	Plume	Thermal
Both momentum and buoyancy	Buoyant jet or forced plume	Buoyant puff

2.4.1 Mechanics of the round jet

An axis-symmetric turbulent jet discharged from a nozzle with exit velocity (U). Here, jet Reynolds number can be defined as $\mathrm{Re} = Ud/\nu$, where d is nozzle diameter and ν is the kinematic viscosity. The transition process of jet can be explained by the schematic of jet as shown in Figure 2.4.

After the flow exits from the nozzle the laminar flow produces the vortex roll-up fairly close to the nozzle. Then amplification involves the formation of a single strength vortex through the vortices paring. A short distance downstream the disturbance causes the vortices to become irregular. Subsequently, the flow breaks down to generate a large number of small scale eddies and becomes fully turbulent flow.

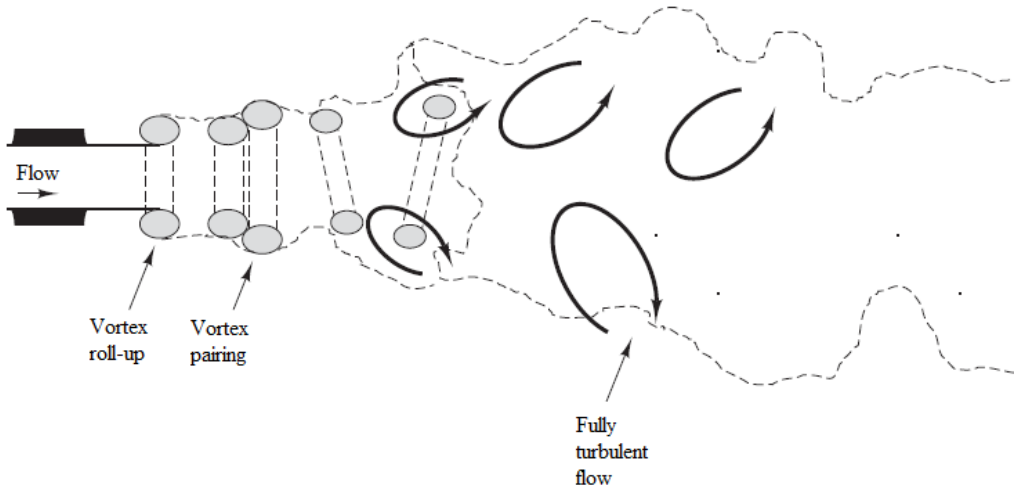

Figure 2.4 Transition in a jet flow [1]

According to the jet flow. There are two important regions, including the potential core or zone of flow establishment (ZFE) and zone of established flow (ZEF) as shown in Figure 2.5. In potential core region, the mean centerline velocity ($\bar{u}_m$) is equal to exit velocity (U). The turbulent mixing does not penetrated into the jet center. However, the mixing process occurs in this region. The large-scale coherent structures (CS) entrain the external fluid into the jet shear layers, which is called bulk mixing, and mixing in smaller-scale dominated by velocity fluctuations [22]. The potential core region or ZFE eventually disappears downstream at distance of between 4-6 times nozzle diameter [23]. The region beyond potential core is called zone of established flow (ZEF). The mixing penetrates into the jet center. The mean velocity ($\bar{u}_m$) founds to decrease with increasing longitudinal distance (x). The cross-sectional velocity profiles show a Gaussian distribution.

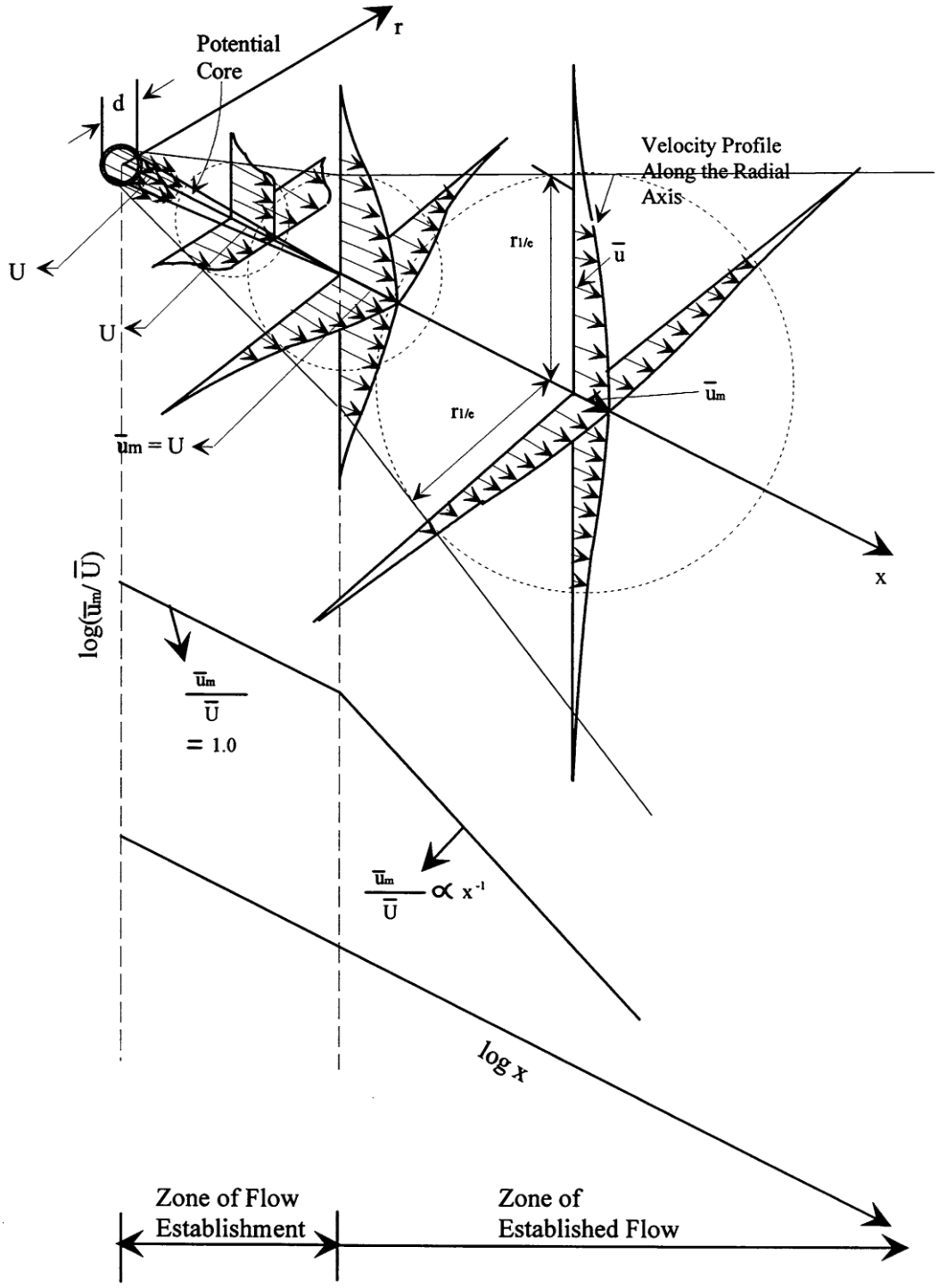

Figure 2.5 Schematic of the round jet [24]

2.4.2 Turbulent jets

Whenever a fluid enters a quiescent body of same fluid, a velocity shear is created between the entering and surrounding fluids, causing turbulence and mixing. Since the properties of turbulent flows depend on the geometry of the flow domain and the type of forces acting on the fluid. The different flow situations require specific investigation. Thus, the basic case of jet penetrating into a quiescent fluid is only considered.

Experimental investigations of jets entering into a quiescent same fluid is shown in Figure 2.6. The radius of jet (R) is proportional to distance (x) downstream from nozzle. The universal angle of jet is 11.8º or approximately 24º from side to opposite side as shown in Figure 2.7. The radius of jet can be calculated by the relation in equation (30). The distance x must be counted from 5d/2 into conduit. This point is called virtual source.

$$R(x) = \frac{1}{5}x \tag{30}$$

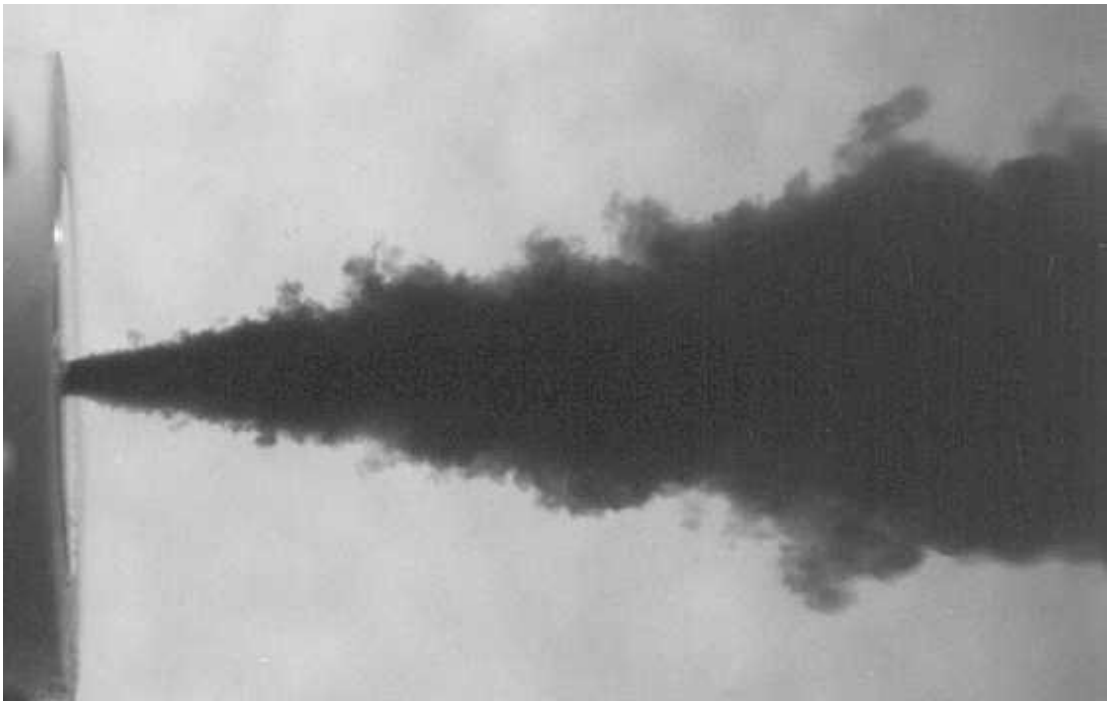

Figure 2.6 A water jet entering from a nozzle into undisturbed tank of water [21]

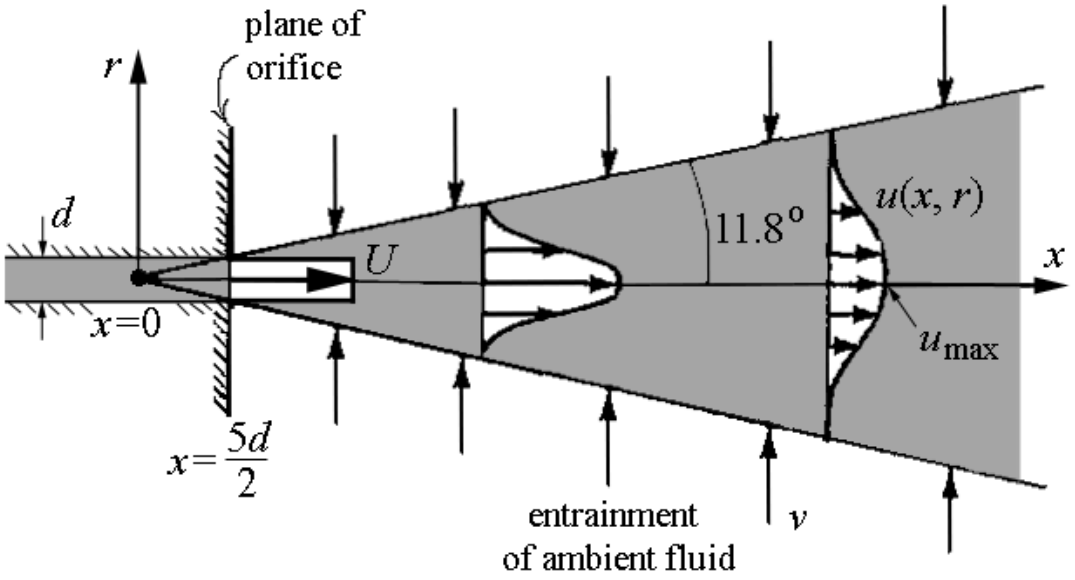

Figure 2.7 Schematic description of a jet penetrating into a quiescent fluid [21]

The velocity profile across the jet exhibits a Gaussian shape (bell shape). Therefore, the velocity profile across the jet is given by

$$u(x,r) = u_{\max} \exp\left(-\frac{50r^2}{x^2}\right) \tag{31}$$

where $u_{\max}(x)$ is maximum velocity at the centerline, r is the radial of jet from centerline, and x is downstream distance along the jet which counted from the virtual source.

When a jet enters a fluid at rest, the only momentum source is the jet itself with absence of external forces (i.e. accelerating force and decelerating force). This means cross-sectional momentum flux of jet remains constant downstream, which is given by

$$\int_0^\infty \rho u^2 2\pi r\,dr = \rho U^2 \frac{\pi d^2}{4} \tag{32}$$

where ρ is fluid density, u is fluid velocity, U is average exit velocity, and d is diameter of nozzle.

After calculating equation (32) and by virtue of equation (31), the result becomes

$$u_{\max} = \frac{5d}{2}U \tag{33}$$

Equation (33) shows that the velocity along jet centerline decrease inversely with distance from virtual source. In other word, the ratio of $U/u_{\max}$ increases linearly with distance (x). The maximum velocity corresponds an average velocity ($\bar{u}$) can be defined as

$$\bar{u} = \frac{1}{\pi R^2}\int_0^{\infty} u 2\pi r dr = \frac{u_{\max}}{2} = \frac{5d}{2x}U \tag{34}$$

According to entrainment of quiescent surrounding fluid, the volumetric flux (Q) is not constant along the jet. The volumetric flux can be expressed as

$$Q = \int_0^{\infty} u 2\pi r dr = \frac{\pi}{50}u_{\max}x^2 = \frac{\pi}{10}dUx \tag{35}$$

The volumetric flux is found to increase linearly with distance (x). The entrainment rate (E) is given by

$$E = \frac{dQ}{dx} = \frac{\pi dU}{10} \tag{36}$$

The entrainment velocity is the radial velocity (v) used to carry this entrainment. The conservation of volume along a section dx of the jet is given by

$$dQ = vdA \tag{37}$$

where v is transverse velocity feeding the entrainment and dA is lateral area of this section of jet ($dA = 2\pi R dx$). Substitution of lateral area and substitution of R in term of x yields

$$\frac{dQ}{dx} = 2\pi R v = \frac{2\pi x v}{5} \tag{38}$$

Substitution equation (38) into equation (36) yields the value of entrainment velocity

$$v = \frac{Ud}{4x} = \frac{u_{\max}}{20} = 0.10\bar{u} \tag{39}$$

The entrainment velocity is found to decrease with distance (x).

2.5 Zinc oxide

2.5.1 Properties of zinc oxide

Zinc oxide is an inorganic chemical compound with formula ZnO. Zinc oxide is insoluble in water. It appears as a white powder as shown in Figure 2.8.

Figure 2.8 Zinc oxide powders
(http://en.wikipedia.org/wiki/File:Zinc_oxide.jpg)

Zinc oxide is n-type semiconductor (II-VI semiconductor). It has several favorable properties, including good transparency, wide band gap energy (3.37 eV), high exciton binding energy (60 meV) and strong room-temperature luminescence. The other properties of zinc oxide are shown in Table 2.3.

Table 2.3 Properties of wurtzite zinc oxide

Property	**Value**
Lattice parameter at 300 K	
a	0.32495 nm
c	0.52069 nm
c/a	1.602 (ideal hexagonal structure is 1.633)
Density	5.606 g/cm^3
Melting point	1975 ºC
Thermal conductivity	130 W/(m·K)
Linear expansion coefficient (/ºC)	a: 6.5×10^{-6}
	c: 3.0×10^{-6}
Static dielectric constant	8.656

Zinc oxide is widely used in various applications, such as plastics, ceramics, glass, cement, lubricants, paints, adhesives, sealants, pigments, foods, batteries, ferrites, fire retardants, first aid tapes, etc.

2.5.2 Synthesis of zinc oxide by thermal oxidation process

The most common process to synthesize zinc oxide is thermal oxidation. Thermal oxidation of zinc vapor provides a highly efficient and simple protocol as it requires only mixing the two feeds of Zn vapor and oxygen in a closed system to allow the oxidation of Zn at a high temperature.

2.6 Literature Reviews

2.6.1 Pulse injection method

Yang et al. [25] synthesized AlN layer using the pulse injection method at 800 ºC. The results was shown that the process parameters in the pulse injection method, including TMAl supply time (τ_{TMAl}), TMAl partial pressure (P_{TMAl}), and 1st H_2 purge time (τ_{H1}) had great influence on the crystal quality and surface morphology. The growth rate, P_{TMAl}, and τ_{H1} should be 1 ML/cycle, 3.91×10^{-4} mbar, and 1 s, respectively. According to these conditions, the best crystal quality were obtained because the agglomeration of grains and gas-phase reaction can be suppressed. TMAl partial pressure should be 3.91×10^{-4} mbar to realize the best quality of AlN layer. Therefore, it can be concluded that the pulse injection method is very effective in achieving high-purity and high-quality AlN layer at temperature of 800 ºC.

2.6.2 Synthesis of zinc oxide by thermal oxidation

Zhang et al. [26] used thermal evaporation technique without presence of catalyst and carrier gas to synthesizes zinc oxide from zinc foils. This experiment was designed to control the growth of the different morphologies of zinc oxide micro- and nano-structures. Their different morphologies, including porous membrane, nanowires (or nanorods), nanobelts, nanoneedles, and tetrapods were depended upon on the different heating rates in a tube furnace.

Hsu et al. [27] synthesized zinc oxide from zinc powder source by thermal evaporation process. Under zinc rich conditions, they observed the large diameter of microwhiskers change to nanoneedles which exhibited strong green defect emission. However, under oxygen rich conditions, the smaller diameter variations were found, and the emission spectrum was dominated by UV instead of defect emission.

Charnhattakorn et al. [14] synthesized zinc oxide nanoparticles with oxygen vacancies by the French process which modified with pulse injection of nitrogen. Nitrogen pulse enhances the reaction between zinc vapor and oxygen in the French process and control oxygen vacancies within zinc oxide nanocrystals. The content of oxygen vacancies depends upon the nitrogen pulse characteristic. The longer nitrogen pulse could provide higher growth of tetrapod zinc oxide with higher oxygen vacancies.

2.6.3 Synthesis of zinc oxide using the combination of experiments and Computational Fluid Dynamics (CFD)

Reuge et al. [4] used a combination of experiments and computational fluid dynamics to studied the chemical vapor synthesis of zinc oxide tetrapods from zinc metal. The commercial CFD code of this research is FLUENT® which based on Finite Volume Method (FVM). The experimental study allowed ultrapure zinc oxide particles with 250-450 nm of mean lengths and 14-27 nm of mean diameters. Zinc oxide nanorods were revealed to depend on the reactor configuration (i.e. parallel flow/cross flow), but not on the position of air injection. However, the yield of the reaction depended both on the reactor configurations and on the position of air injection. It was maximum for the cross flow configurations. The CFD successfully predicted the experimental yield of the reaction for all the conditions tested. The combination of the experimental and simulated results led to better understanding of heat and mass transfer. For the several parameters, such as argon and air flow rates, position of air injection, etc., were varied in the simulation to find the optimized reaction conditions for maximum yield and production rate. For cross flow configuration, the simulation results showed 71% yield and a production rate 7 times higher than the nominal value have been obtained.

Yamamoto et al. [15] fabricated tetrapod zinc oxide nanoparticles by gas phase reaction with using flow restrictor and integrated computational fluid dynamics to analyzed the phenomena inside the reactor. For flow restrictor, the leaving sufficient amounts of unreacted Zn vapor formed tetrapod zinc oxide. The simulated results showed the flow restrictor suppresses the mixing and reduces the residence time in the reactor so the remaining unreacted Zn vapor allowed the zinc oxide particles to grow in tetrapod-shape.

CHAPTER III

SIMULATION

Procedures of simulation are described in this chapter. This simulation research is based on the experimental work of zinc oxide synthesis from zinc foils by thermal oxidation process reported by Charnhattakorn et al. [14]. Based on our literature survey, the following simulation procedures are designed as a tentative guideline. Simulation works would be separated into 3 parts; which are (i) Model setup, (ii) Investigation of grid independent solutions (iii) Validation of the model, and (iv) Simulation of synthesis parameters which effect on yields of zinc oxide.

3.1 Model setup

3.1.1 Modeling of zinc oxide reactor

This simulation were set up based on the experimental work which reported by Charnhattakorn et al. [14]. The system is a tubular reactor with length of 650 mm and inner diameter of 42 mm. The reactor was equipped with a coaxial tube at the upstream of the reactor for the delivery of air and nitrogen carrier gas to the reactor and a tube at another end for supplying a pulsing gas to the reaction zone as shown in Figure 3.1.

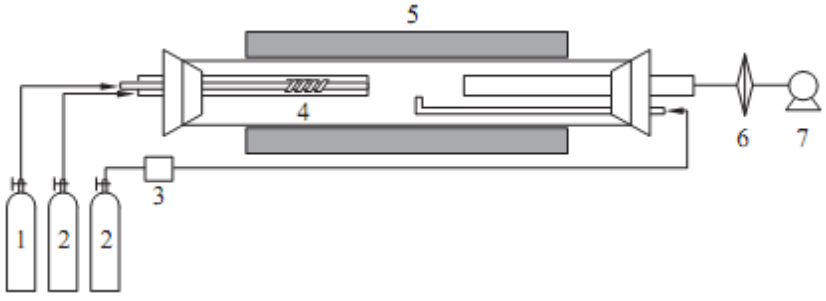

Figure 3.1 Schematic diagram of experiment of Charnhattakorn et al. [14] : (1) supplied air, (2) supplied nitrogen gas, (3) solenoid valve controlled by timer, (4) zinc foil, (5) electrical furnace, (6) filter, and (7) vacuum pump

This reactor system was simplified to be two-dimensional as shown in Figure 3.2. The calculation domain and grid generation was done by GAMBIT as shown in Figure 3.3.

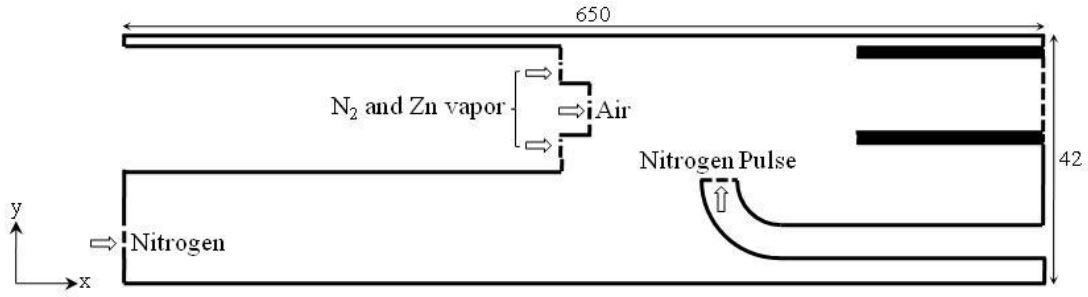

Figure 3.2 Calculation domain

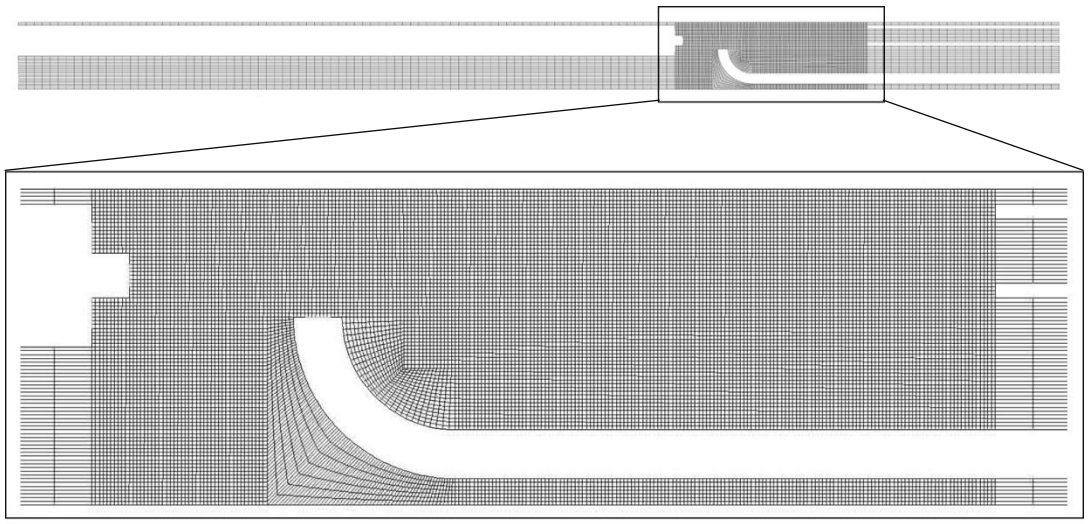

Figure 3.3 Gird generation of calculation domain

3.1.2 Boundary conditions

The boundary conditions were referred to experimental research of Charnhattakorn et al. [14]. Velocity profiles of gas at inlet were assumed to be uniform flow. The inlet gas velocities are shown in Table 3.1. Nitrogen pulse was applied to generate turbulence which enhanced mixing of zinc vapor and oxygen as depicted in Figure 3.4. At the walls, no-slip boundary condition was assumed while a temperature profile as shown in Figure 3.5 was applied along the longitudinal distance. The nitrogen pulse velocity and temperature profile along longitudinal distance were written in the C programming language and then applied to the solver.

Table 3.1 Inlet gas velocities

Feed	**Velocity, (m/s)**
Air	1.532
Nitrogen	0.628
Nitrogen and Zn vapor	0.166
Nitrogen Pulse	Figure 3.4

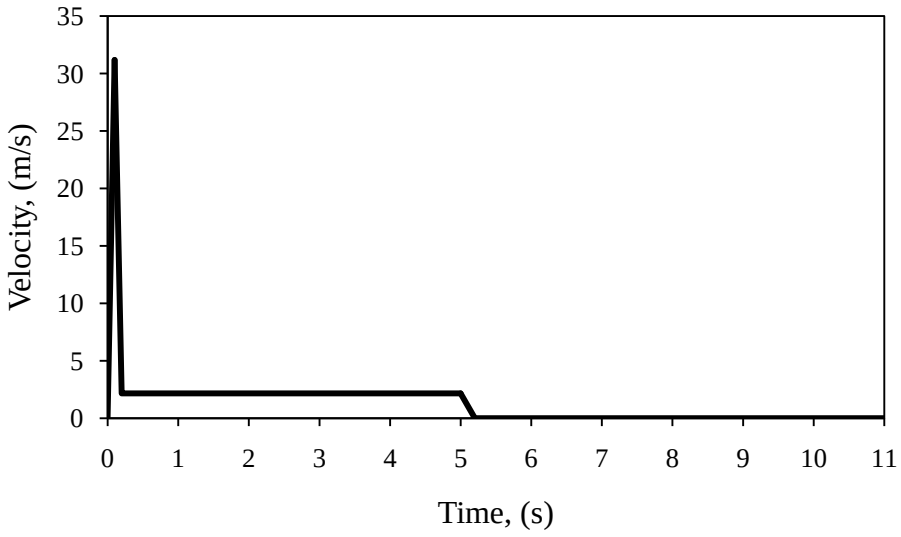

Figure 3.4 Time dependence of nitrogen pulse velocity

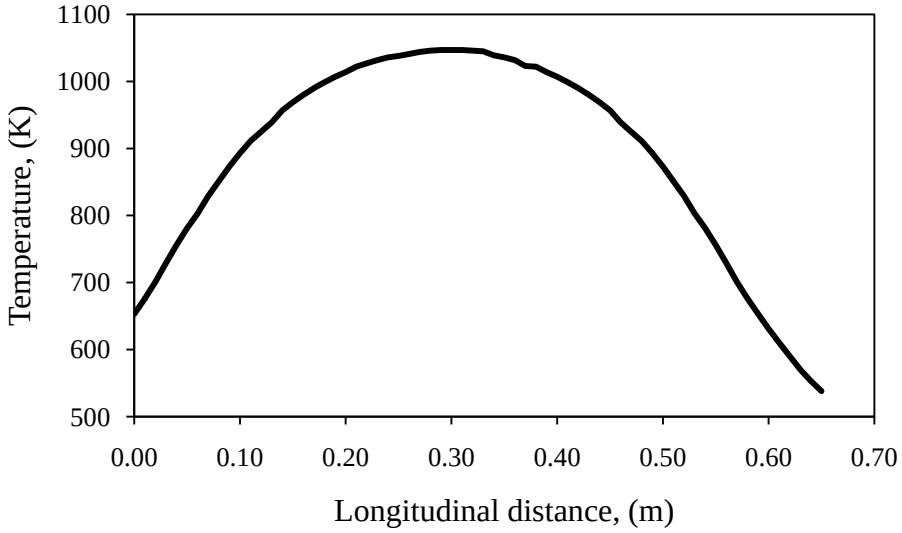

Figure 3.5 Temperature profile along the longitudinal distance

3.1.3 Assumptions of the model

The first assumption of the model was two-dimensional flow. Gases were considered to be ideal gas. Regarding to the general rule of thumb, gases were considered to be incompressible because Mach number was less than 0.2 [28]. The Fluid motion in the reactor was assumed to be turbulent flow. The homogeneous gas phase reaction was only considered.

3.1.4 Governing equations of the model

According to the assumptions of the model, the governing equations of the model, including continuity equation, momentum equations, energy equation, k-epsilon turbulence model, and species transport equations with finite reaction rate can be expressed as follows,

continuity equation:

$$\frac{\partial \bar{u}}{\partial x} + \frac{\partial \bar{v}}{\partial y} = 0 \qquad (40)$$

momentum equation in x-direction:

$$\rho\left(\frac{\partial \bar{u}}{\partial t}+\frac{\partial\left(\bar{u}^{2}\right)}{\partial x}+\frac{\partial(\bar{v}\bar{u})}{\partial y}\right)=-\frac{\partial \bar{p}}{\partial x}+\frac{\partial}{\partial x}\left(\mu_{eff}\,\frac{\partial \bar{u}}{\partial x}\right)+\frac{\partial}{\partial y}\left(\mu_{eff}\,\frac{\partial \bar{u}}{\partial y}\right) \tag{41}$$

momentum equation in y-direction:

$$\rho\left(\frac{\partial \bar{v}}{\partial t}+\frac{\partial(\bar{u}\bar{v})}{\partial x}+\frac{\partial\left(\bar{v}^{2}\right)}{\partial y}\right)=-\frac{\partial \bar{p}}{\partial y}+\frac{\partial}{\partial x}\left(\mu_{eff}\,\frac{\partial \bar{v}}{\partial x}\right)+\frac{\partial}{\partial y}\left(\mu_{eff}\,\frac{\partial \bar{v}}{\partial y}\right)-\rho g \tag{42}$$

energy equation:

$$\frac{\partial}{\partial t}(\rho E)+\frac{\partial}{\partial x_i}\left[\overline{u_i}(\rho E+\bar{p})\right]=\frac{\partial}{\partial x_j}\left(k_{eff}\,\frac{\partial T}{\partial x_j}+\overline{u_i}\left(\tau_{ij}\right)_{eff}\right)+S_h \tag{43}$$

where $k_{eff}=k+\dfrac{c_p\mu_t}{\mathrm{Pr}_t}$ and $\left(\tau_{ij}\right)_{eff}=\mu_{eff}\left(\dfrac{\partial \overline{u_j}}{\partial x_i}+\dfrac{\partial \overline{u_i}}{\partial x_j}\right)-\dfrac{2}{3}\mu_{eff}\,\dfrac{\partial \overline{u_k}}{\partial x_k}\delta_{ij}$.

k-transport equation:

$$\frac{\partial}{\partial t}(\rho k)+\frac{\partial}{\partial x_i}\left(\rho k\overline{u_i}\right)=\frac{\partial}{\partial x_j}\left[\left(\mu+\frac{\mu_t}{\sigma_k}\right)\frac{\partial k}{\partial x_j}\right]+G_k+G_b-\rho\varepsilon-Y_M+S_k \tag{28}$$

ε -transport equation:

$$\frac{\partial}{\partial t}(\rho\varepsilon)+\frac{\partial}{\partial x_i}\left(\rho\varepsilon\overline{u_i}\right)=\frac{\partial}{\partial x_j}\left[\left(\mu+\frac{\mu_t}{\sigma_\varepsilon}\right)\frac{\partial \varepsilon}{\partial x_j}\right]+C_{1\varepsilon}\frac{\varepsilon}{k}\left(G_k+C_{3\varepsilon}G_b\right)-C_{2\varepsilon}\rho\frac{\varepsilon^2}{k}+S_\varepsilon \tag{29}$$

species transport equations:

$$\frac{\partial}{\partial t}\left(\rho Y_i\right)+\frac{\partial}{\partial x_i}\left(\rho Y_i\overline{\mathbf{U}}\right)=-\frac{\partial \overrightarrow{J_i}}{\partial x_j}+R_i+S_i \tag{44}$$

where $\overrightarrow{J_i}=-\left(\rho D_{i,m}+\dfrac{\mu_t}{\mathrm{Sc}_t}\right)\nabla Y_i-D_{T,i}\dfrac{\nabla T}{T}$

In thermal oxidation process, zinc vapor is oxidized according to the following homogeneous gas phase reaction.

$$\mathrm{Zn} + \frac{1}{2}\mathrm{O_2} \xrightarrow{k^{\mathrm{hom}}} \mathrm{ZnO(g)} \tag{45}$$

The reaction rate of this reaction can be expressed as the following relation.

$$-\mathrm{r_{Zn}} = \mathrm{r_{ZnO}} = \mathrm{k_0}[\mathrm{Zn}][\mathrm{O_2}]^{1/2} \tag{46}$$

$$\mathrm{k_0} = 8.0\times10^{8}\exp\left(-\frac{1.29\times10^{8}}{\mathrm{RT}}\right)\mathrm{m^{3/2}\cdot mol^{-1/2}\cdot s^{-1}} \tag{47}$$

where R is the universal gas constant and T is the reaction temperature.

3.1.5 Numerical methods

Governing equations have been solved numerically by using FLUENT® with finite volume method (FVM), in which the computation domain is divided into a number of small cells, and the partial differential equations are integrated over each cell to obtain a set of algebraic equations. These algebraic equations were solved iteratively to obtain the field distribution of dependent variables. For this study, the pressure-velocity coupling was solved by using SIMPLE algorithm. The spatial discreatisation of gradient and pressure were least squares cell based and standard, respectively. Second order upwind scheme was applied to calculate momentum, energy, and gas species. The other quantities were calculated by first order upwind discreatisation scheme.

3.2 Investigation of grid independent solutions

The purpose of this step was to make CFD calculations that gave grid independent solutions, i.e. results that do not change when the grid is refined further. The grid independent solution can be defined as a solution that has a solution error that is within a range that can be accepted by the researcher [29].

The procedure of grid independent solutions can be summarized as a diagram shown in Figure 3.6.

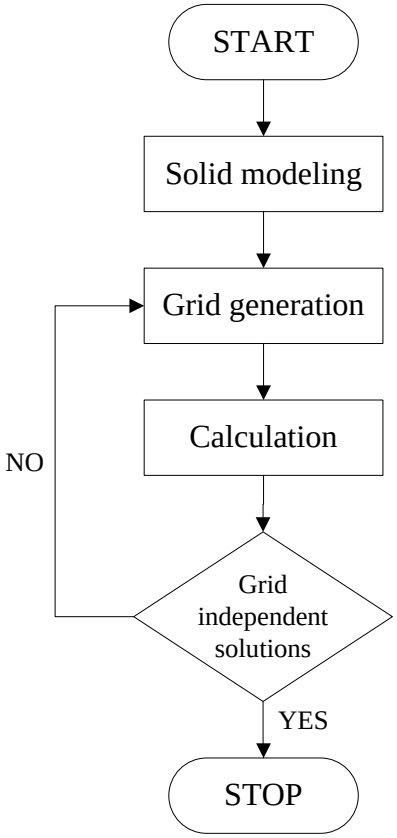

Figure 3.6 Investigation procedure of grid independent solution

3.3 Validation of the model

Validation can defined as a process for assessing simulation modeling uncertainty by using benchmark experimental data [30]. The simulation results of three different pulse injection positions, including 0.5, 2.5, and 5.5 cm, were validated by comparing with experimental results which reported by Charnhattakorn et al. [14]. The pulse injection position can be defined as the distance between the exit of air feed and the center of nitrogen pulse injection position (x_{pulse}) as shown in Figure 3.7.

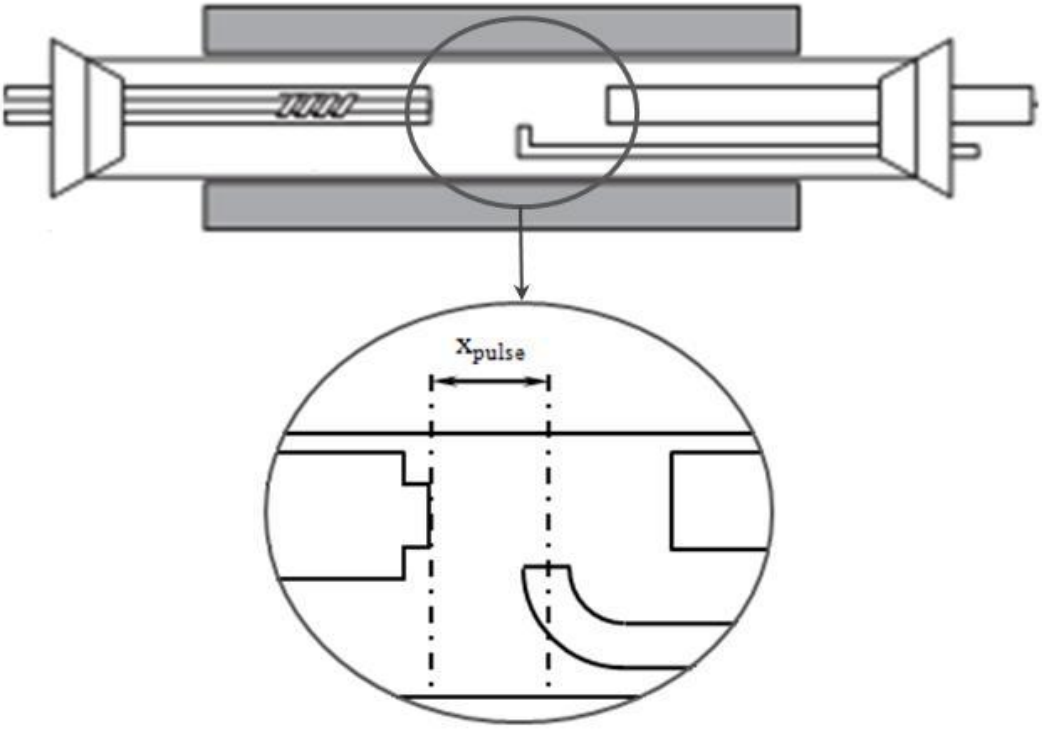

Figure 3.7 Pulse injection position

3.4 Simulation of synthesis parameters which affect the yield of zinc oxide

The investigation of this simulation was separated into three parts as follow.

3.4.1 Effect of pulse injection position

In this part, the effect of the pulse injection position on yields of zinc oxide was investigated by varying the Reynolds numbers of air jet, including Re of 315 which was the same value as that in the validation case, and Re of 630. The inlet gas velocities are shown in Table 3.2.

Table 3.2 Inlet gas velocities for two different Reynolds numbers

Feed	**Velocity, (m/s)**	
	Re=315	**Re=630**
Air	1.532	3.064
Nitrogen	0.628	0.628
Nitrogen and Zn vapor	0.166	0.166
Nitrogen Pulse	Figure 3.4	Figure 3.4

3.4.2 Effect of pulse characteristic

The effect of pulse characteristic, including pulse nitrogen injection, and continuous nitrogen injection, on yields of zinc oxide was investigated. The total mass of cross flow nitrogen of both characteristics were identical. The inlet gas velocities are shown in Table 3.3.

Table 3.3 Inlet gas velocities for two different pulse characteristics

Feed	**Velocity, (m/s)**	
	Pulse	**Continuous**
Air	1.532	1.532
Nitrogen	0.628	0.628
Nitrogen and Zn vapor	0.166	0.166
Nitrogen Pulse	Figure 3.4	1.258

3.4.3 Effect of air feed position

The effect of two different air feed positions, including co-current with continuous nitrogen flow, and cross current, on production yields were investigated. For cross current, nitrogen pulse and air were fed at air feed tube and nitrogen pulse tube, respectively. The inlet gas velocities are shown in Table 3.4.

Table 3.4 Inlet gas velocities for two different air feed positions

Feed	**Velocity, (m/s)**	
	Co-current	**Cross current**
Air	1.532	1.126
Nitrogen	0.628	0.628
Nitrogen and Zn vapor	0.166	0.166
Nitrogen Pulse	1.258	1.533

CHAPTER IV

RESULTS AND DISCUSSION

4.1 Investigation of grid independent solutions

In this part, the reactor with x_{pulse} of 2.5 cm was only modeled to examine grid independent solutions. All models were done by GAMBIT. The geometry was separated into three parts, including upstream zone, reaction zone, and outlet zone as shown in Figure 4.1. Grid generation of all models was controlled to be quad cell as shown in Figure 4.2.

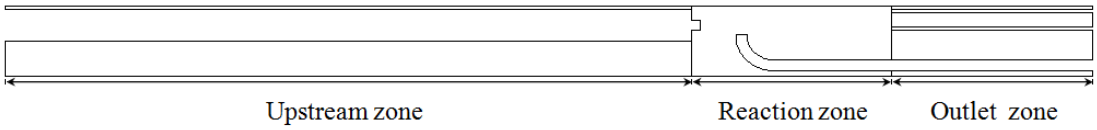

Figure 4.1 Geometry of the model

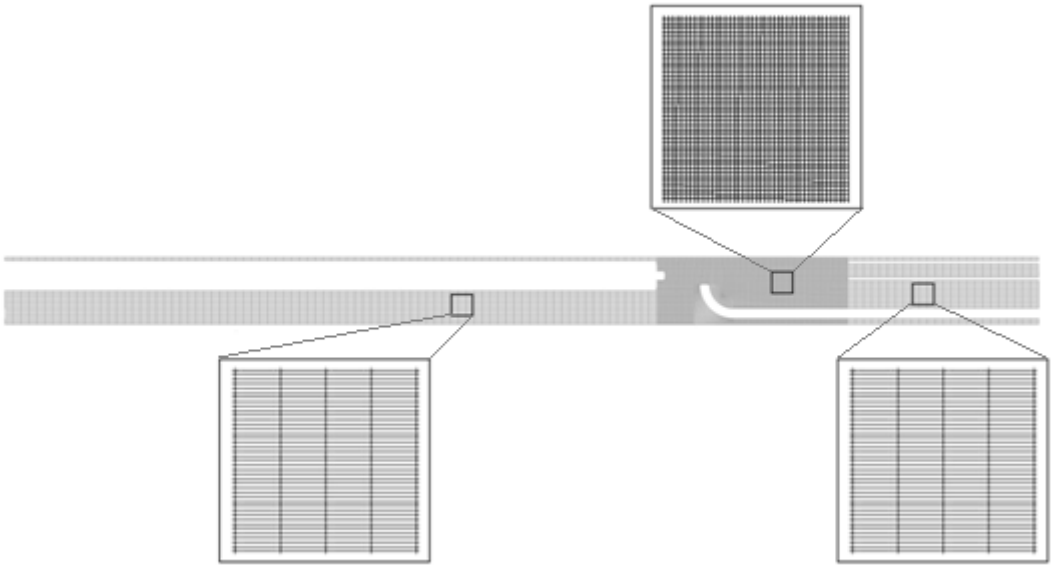

Figure 4.2 Grid generation of the model

Grid size was varied from 0.5 to 0.09 mm to determine grid independent solution as shown in Figure 4.3. The information of grid quality and grid quantity is shown in Table 4.1.

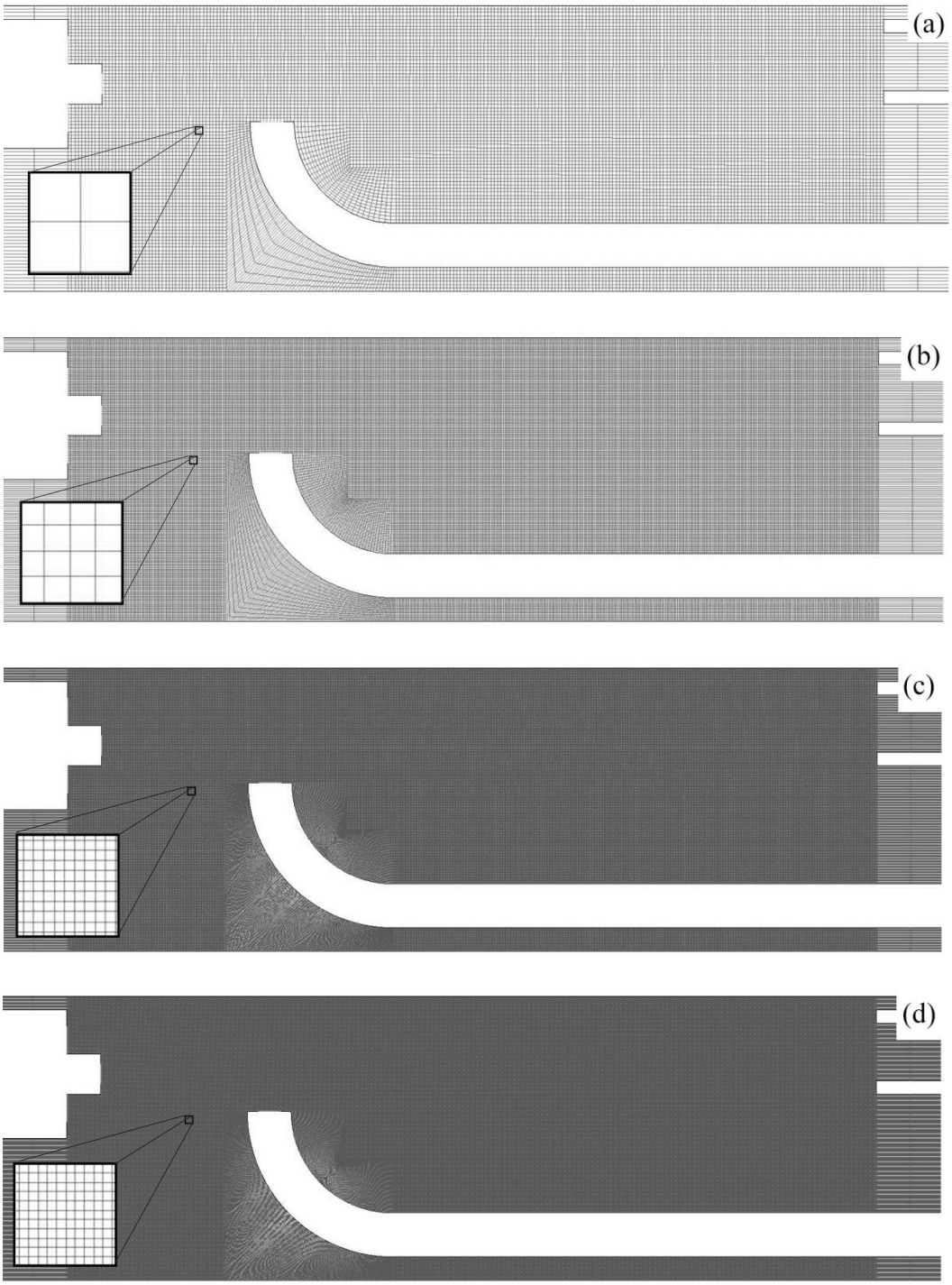

Figure 4.3 Grid generation of the model with x_{pulse} equal to 2.5 cm and grid size varied from: (a) 0.5, (b) 0.25, (c) 0.1, and (d) 0.09 mm

Table 4.1 Grid quality and grid quantity for different grid size

Size (mm)	Grid quality		Grid quantity	
	Minimum Orthogonal	**Maximum Aspect Ratio**	**Cells**	**Nodes**
0.5	7.08×10^{-1}	10	22,380	23,184
0.25	7.07×10^{-1}	20	78,577	79,920
0.1	7.07×10^{-1}	50	452,994	455,963
0.09	7.07×10^{-1}	55	553,627	556,894

The calculated yields of zinc oxide were compared with the experimental results as shown in Table 4.2. The simulation results showed that grid independent solution was obtained at number of grid cells equal to 452,994 (grid size of 0.1 mm) as shown in Figure 4.4.

Table 4.2 Comparison between experimental yields of zinc oxide and simulated data

Experimental yield of zinc oxide (%)	Simulation yield of zinc oxide (%)			
	0.5 mm	**0.25 mm**	**0.1 mm**	**0.09 mm**
32.24	16.78	20.87	31.38	30.69

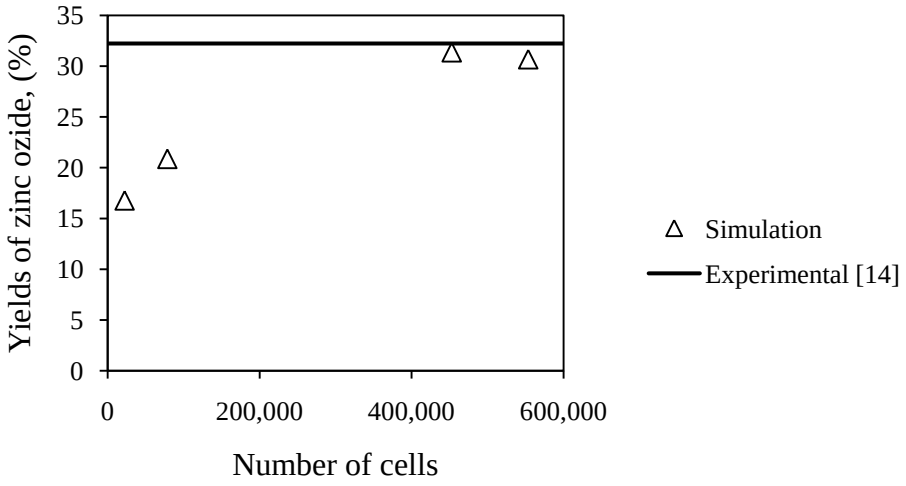

Figure 4.4 The simulated yields of zinc oxide with different number of grid cells

According to grid independent study, the other models were generated with grid size of 0.1 mm.

4.2 Validation of the model

According to the grid independent solution, all models to study three different pulse injection positions were done by GAMBIT with the grid size of 0.1 mm. Here, the dimensionless distance of pulse injection position (x^*_{pulse}) was introduced. The dimensionless x^*_{pulse} was defined as the ratio of the distance between the exit of air feed and the center of nitrogen pulse injection position (x_{pulse}), (i.e., 0.5, 2.5, and 5.5 cm) to 0.3 cm air feed tube diameter (d_{air}). Grid generation of these models and their descriptions of grid quality and grid quantity are shown in Figure 4.5 and Table 4.3, respectively.

The synthesis of zinc oxide by thermal oxidation was simulated using FLUENT® software. The k-epsilon model was used to model turbulence, and species mass transport equations with finite rate with eddy dissipation were employed to calculate mass transport of zinc oxide. The boundary conditions (i.e., inlet velocity, temperature, and mass fraction) of all models referred to the experimental work of Charnhattakorn et al. The simulated results were validated by comparing with the experimental results reported by Charnhattakorn et al. [14].

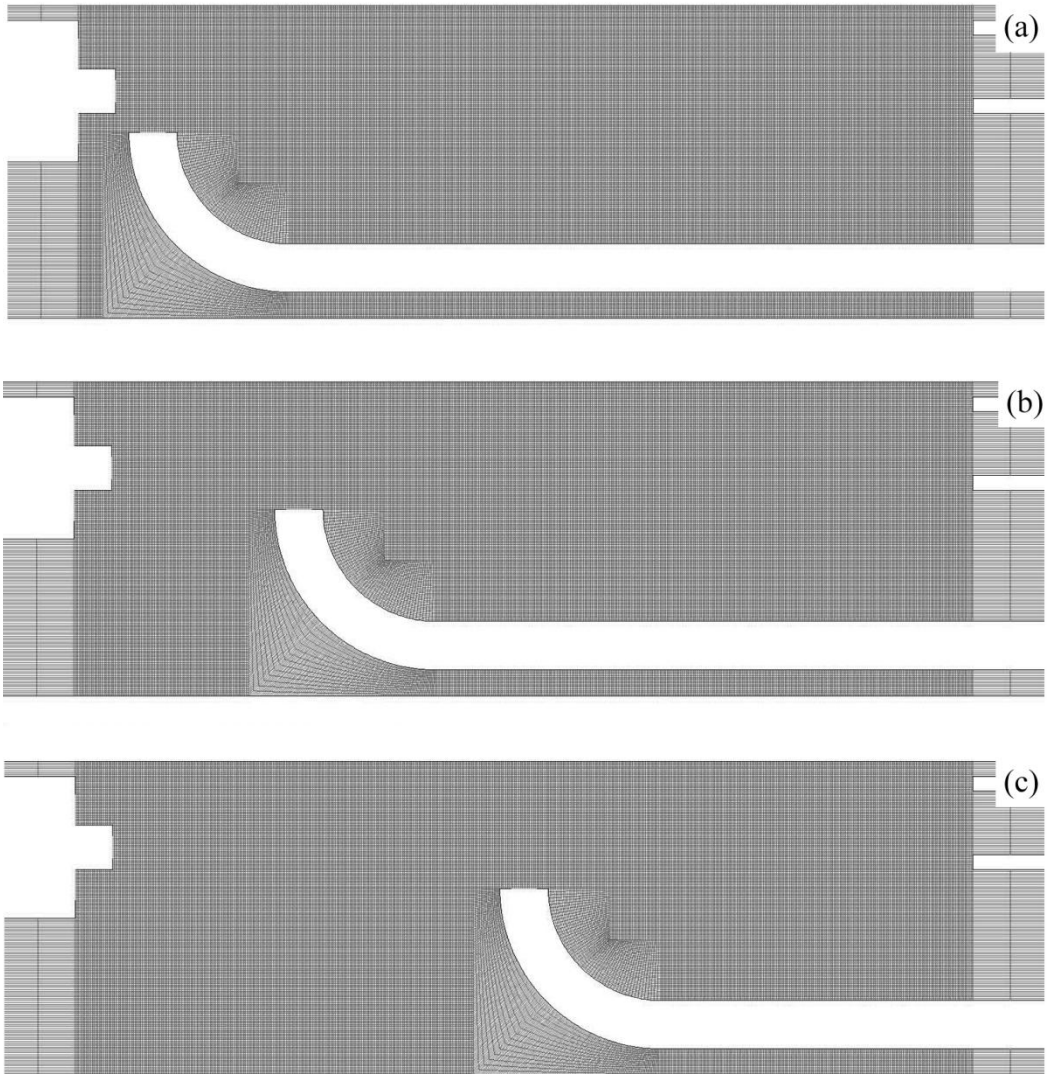

Figure 4.5 Grid generation of the model for x^*_{pulse} of: (a) 1.67, (b) 8.33, and (c) 18.33

Table 4.3 Grid quality and grid quantity for different x^*_{pulse}

x^*_{pulse}	Grid quality		Grid quantity	
	Minimum Orthogonal	**Maximum Aspect Ratio**	**Cells**	**Nodes**
1.67	7.07×10^{-1}	50	437,992	441,162
8.33	7.07×10^{-1}	50	452,994	455,963
18.33	7.07×10^{-1}	50	472,286	474,956

The main assumption of k-epsilon model is isotropic. This model does not account either large-scale or small-scale of turbulence. According to this assumption, the model constants of finite rate with eddy dissipation were modified to obtain the yield of zinc oxide. The mixing constant A for x^*_{pulse} of 1.67, 8.33, and 18.33 were 0.375, 4, and 0.5, respectively. The constant B for x^*_{pulse} of 1.67, 8.33, and 18.33 were 0.1, 0.5, and 0.1, respectively.

The simulation results were obtained for three different x^*_{pulse}, including 1.67, 8.33, and 18.33. Figure 4.6 illustrates the comparison between the computed yields of zinc oxide and the experimental data for different x^*_{pulse}. Figure 4.7 shows contours of velocity and mass fraction of zinc oxide for different x^*_{pulse} at t=11.1s.

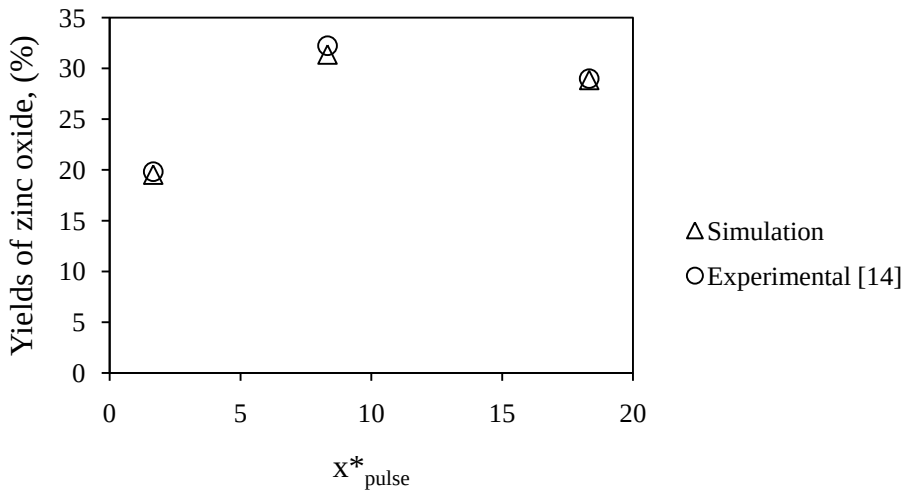

Figure 4.6 Comparison between simulated yields of zinc oxide and experimental data for different x^*_{pulse}

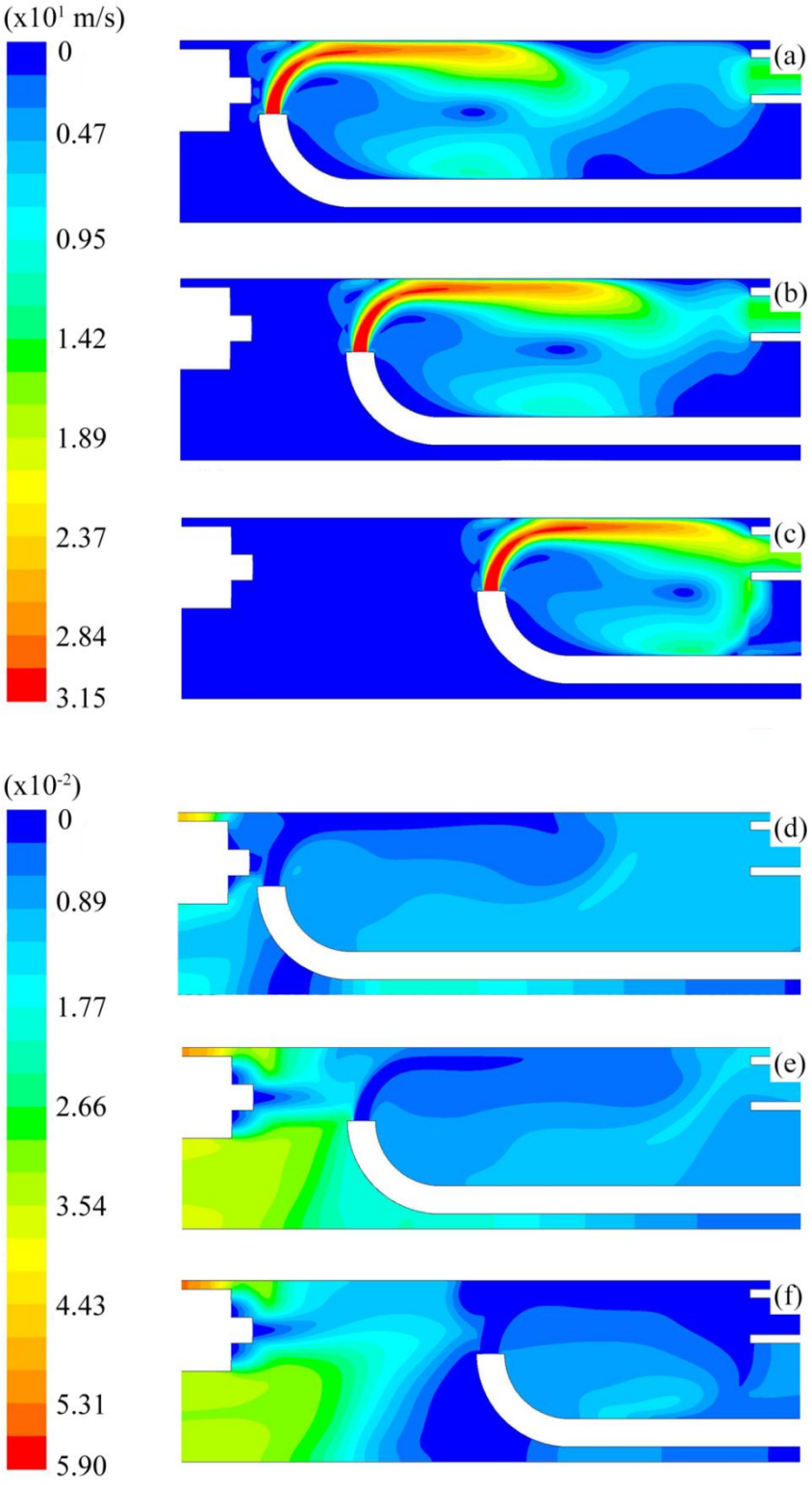

Figure 4.7 The contours of velocity for x^*_{pulse} of: (a) 1.67, (b) 8.33, and (c) 18.33 and the mass fraction of zinc oxide contours for x^*_{pulse} of: (d) 1.67, (e) 8.33, and (f) 18.33 at t=11.1s

The contours of velocity, mass fraction of zinc oxide and temperature for x^*_{pulse} of 8.33 at t=11.1s and t=19s are shown in Figure 4.8 and Figure 4.9, respectively.

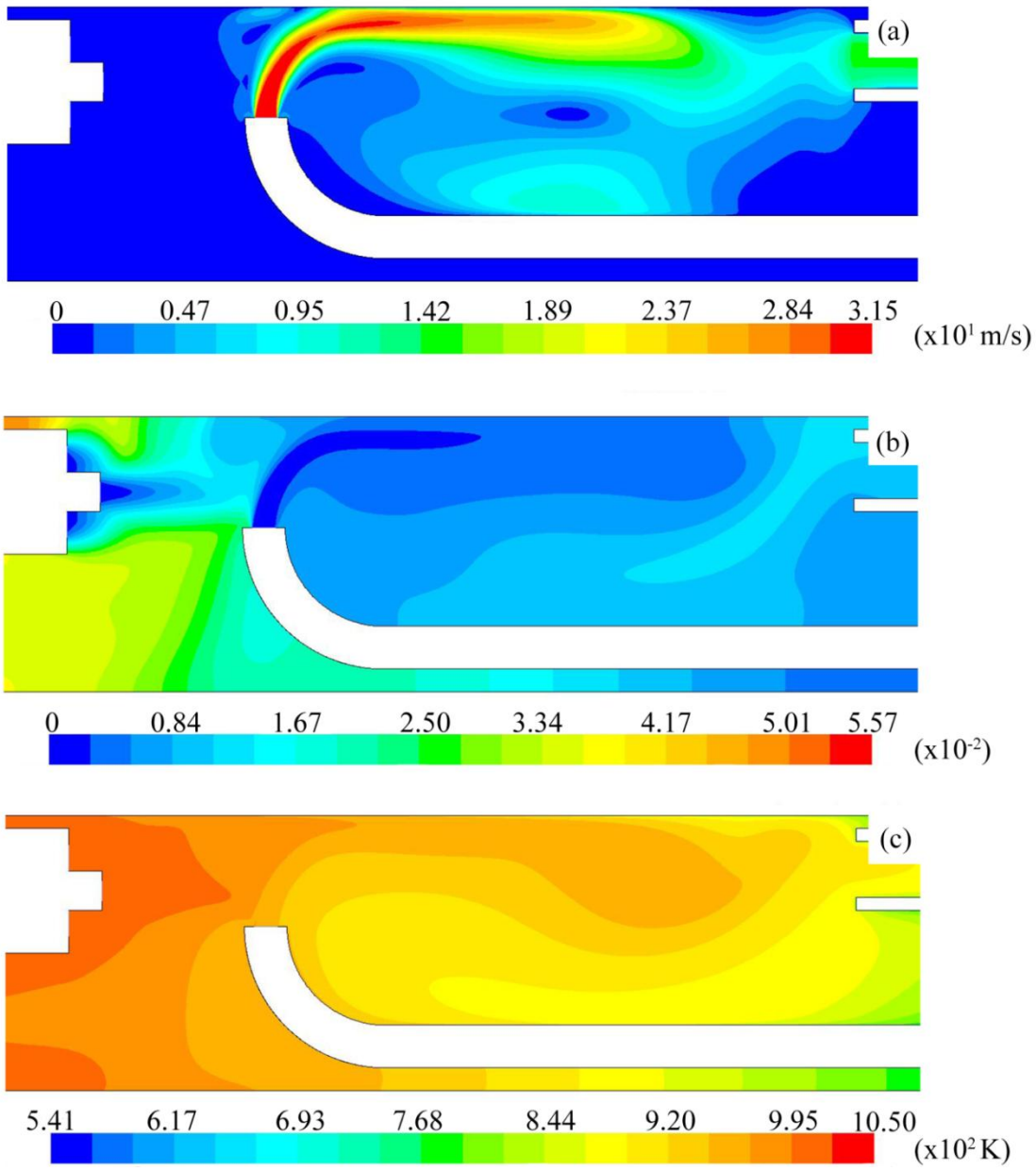

Figure 4.8 The contours of: (a) velocity, (b) mass fraction of zinc oxide, and (c) temperature, for x^*_{pulse} of 8.33 at t=11.1s

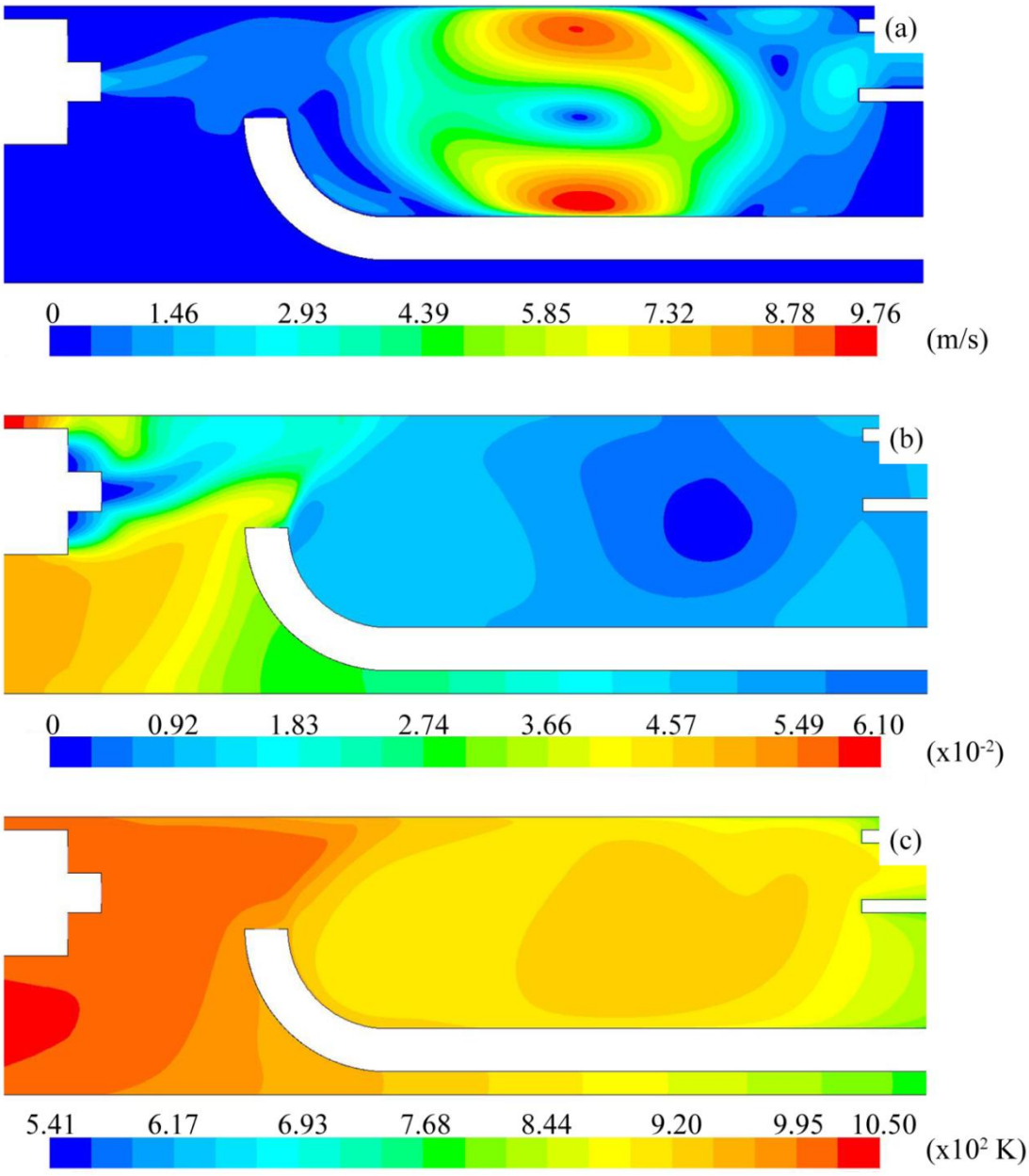

Figure 4.9 The contours of: (a) velocity, (b) mass fraction of zinc oxide, and (c) temperature, for x^*_{pulse} of 8.33 at t=19s

The error between the predicted yields of zinc oxide and the experimental data was less than 3% as shown in Table 4.4. Based on the results in Figure 4.6 and Table 4.4, the computed yields of zinc oxide were in good agreement with the experimental data.

Table 4.4 Summary of the experimental and simulation results for different x^*_{pulse}

x^*_{pulse}	Experimental yield (%)	Simulated yield (%)	% error
1.67	19.82	19.53	1.46
8.33	32.24	31.38	2.69
18.33	29	28.87	0.46

4.3 Simulation of synthesis parameters which affect the yield of zinc oxide

4.3.1 Effect of pulse injection position

The experimental and simulation results showed that the maximum yield of zinc oxide was observed at x^*_{pulse} of 8.33. The cause of the presence of maximum zinc oxide yield would be ascribed to the influence of air jet. Such effect was confirmed by varying two different Reynolds numbers of air jet (Re_{air}), including Re_{air} of 315, which was the same value as that in the validation case, and Re_{air} of 630. Here, Reynolds number of air jet can be defined as $Re_{air} = Ud_{air} / \nu_{air}$, U is average air exit velocity, d_{air} is air feed tube diameter, and ν_{air} is kinematic viscosity of air. These two different models were simulated without nitrogen pulse injection. The contours of axial velocity of air jet for two different Reynolds numbers are shown in Figure 4.10.

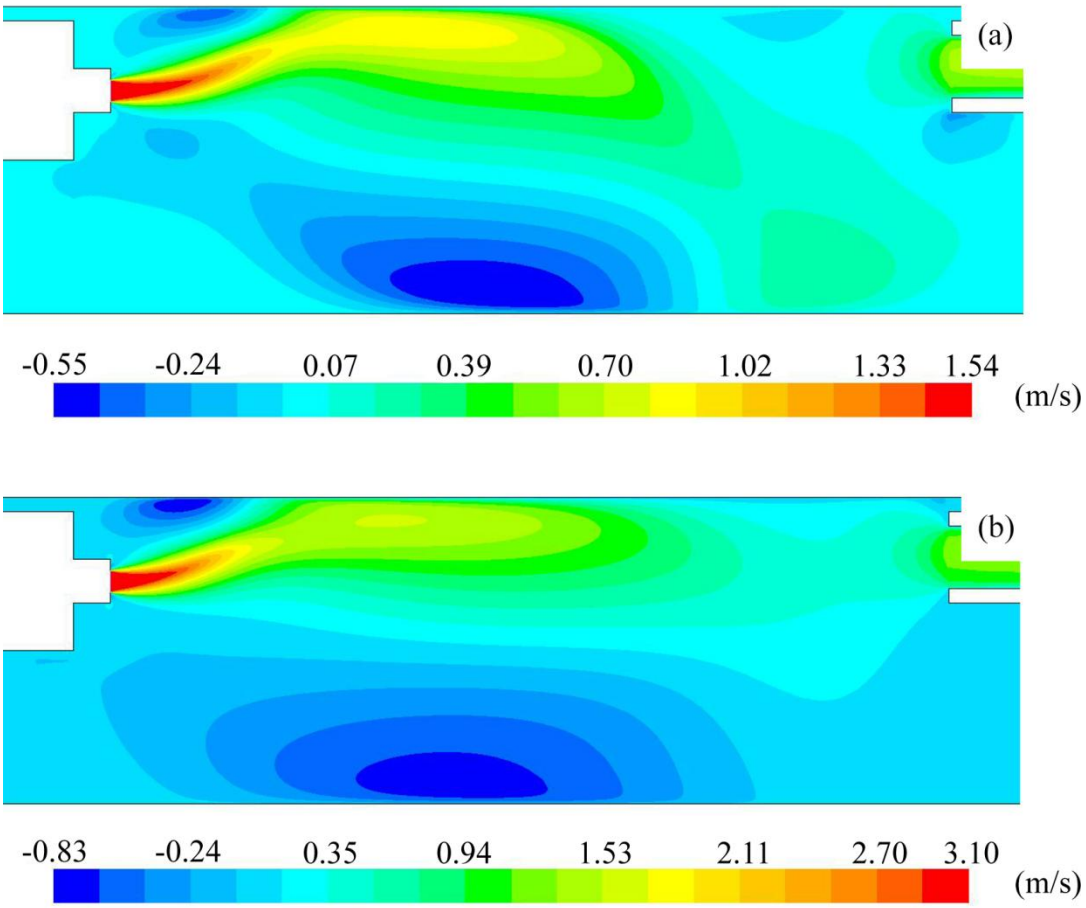

Figure 4.10 Axial velocity contours of: (a) Re_{air}=315 and (b) Re_{air}=630

Regarding to the jet flow, jet consists of two important regions, including zone of flow establishment (ZFE), and zone of established flow (ZEF). In potential core region or ZFE, the mean centerline velocity is equal to air exit velocity (U). The cross-sectional axial velocity distributions of air jet at different x^*_{air} showed that the ZFE region were observed to disappear at x^*_{air} of 4 as shown in Figure 4.11. The dimensionless x^*_{air} can be defined as the ratio of longitudinal distance from air exit (x) to air feed tube diameter (d_{air}).

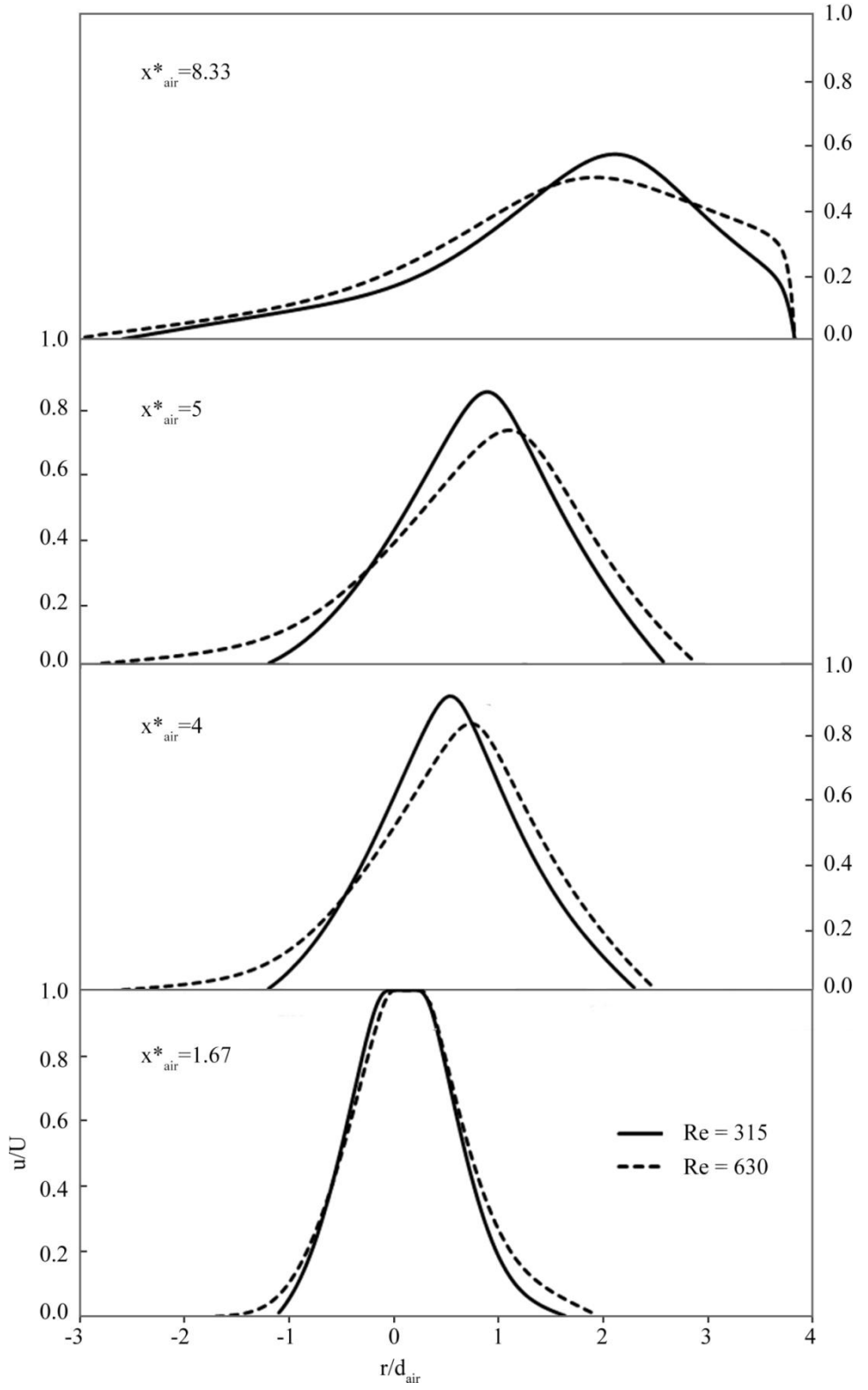

Figure 4.11 The relation between ratio of cross-sectional axial velocity of air jet to air exit velocity (u/U) and the ratio of radius from centerline of air tube to air feed tube diameter (r/d_{air}) for different x^*_{air}

The second important region is called zone of established flow (ZEF), in which the turbulent mixing penetrates into the jet center. In other words, the environmental fluid is entrained by jet stream. Typically, the maximum entrainment velocity occurs at the first position of turbulent region. The maximum entrainment velocity of two different air Reynolds numbers, including 315, and 630, occurred at x^*_{air} of 8.33 and 5, respectively, as shown in Figure 4.12. In other words, The first position of turbulent flow of two different Reynolds numbers, including 315, and 630, occurred at x^*_{MEV} of 8.33 and 5, respectively. The dimensionless distance of maximum entrainment velocity position (x^*_{MEV}) can be defined as the ratio of the position with the maximum entrainment velocity (x_{MEV}) to air feed tube diameter (d_{air}).

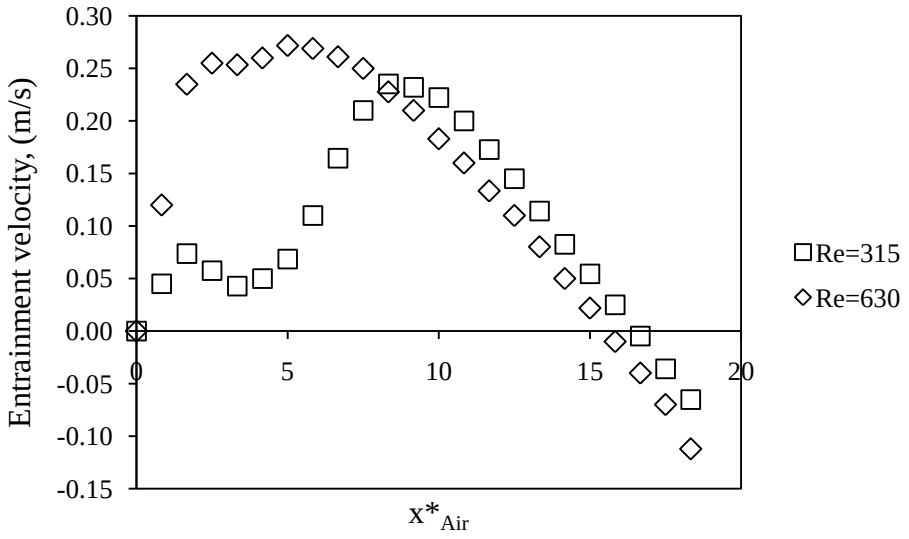

Figure 4.12 Entrainment velocity along x^*_{air}

The yields of zinc oxide for air Reynolds number of 630 with six different pulse injection positions (x^*_{pulse}), including 1, 1.67, 5, 8.33, 11, and 18.33, were simulated. These six models were separated into two groups. The first group (Group I) was referred to the same positions in validation case, including 1.67, 8.33, and 18.33. The second group (Group II), including 1, 5, and 11 was referred to the same positions of x* in validation case. The dimensionless x* can be defined as the ratio of the dimensionless of pulse injection position (x^*_{pulse}) to the dimensionless

distance of the maximum entrainment velocity position (x^*_{MEV}) for given Reynolds number. Grid generation of these models and their descriptions of grid quality and grid quantity are shown in Figure 4.13 and Table 4.5, respectively.

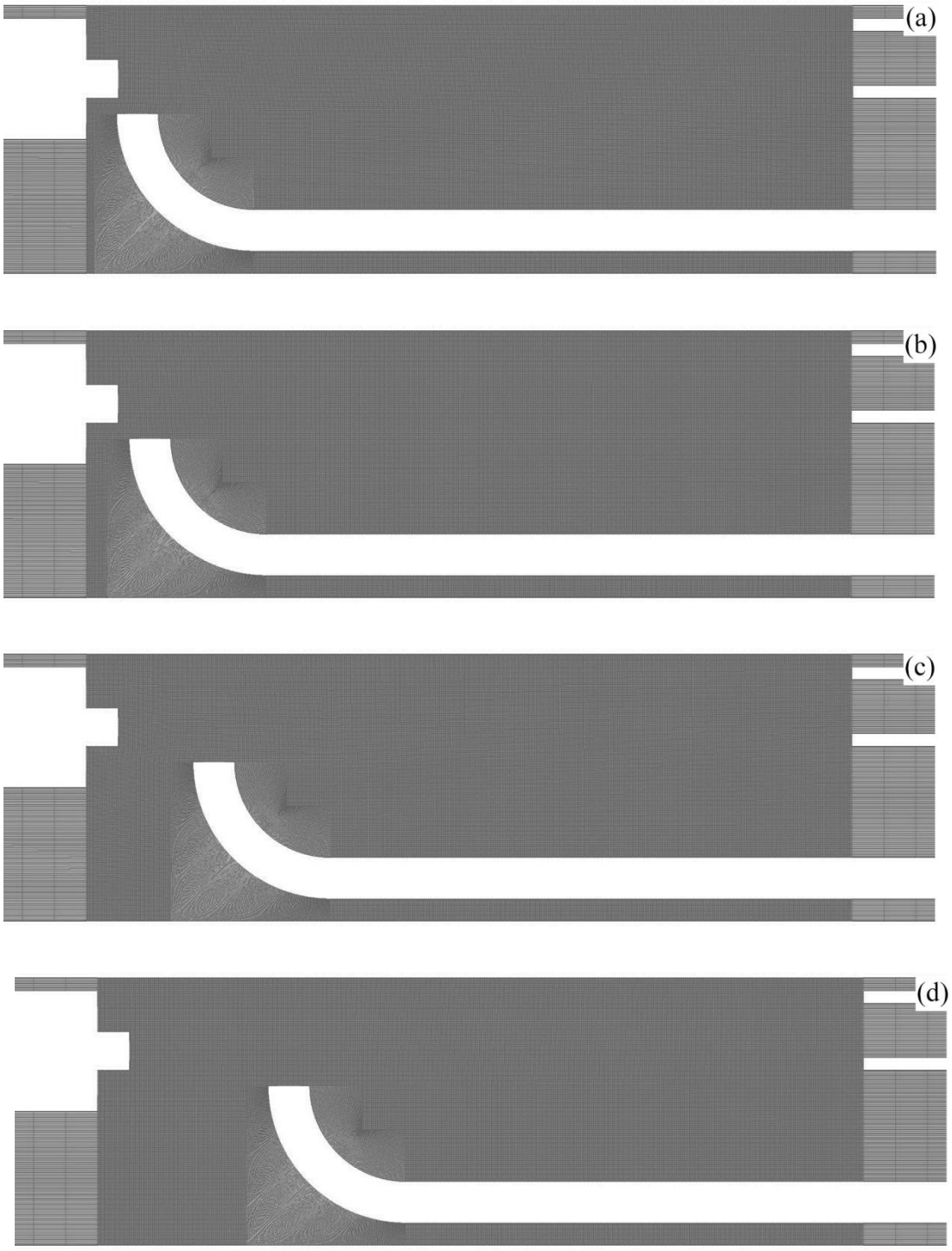

Figure 4.13 Grid generation of the model for x^*_{pulse} of: (a) 1, (b) 1.67, (c) 5, (d) 8.33, (e) 11, and (f) 18.33

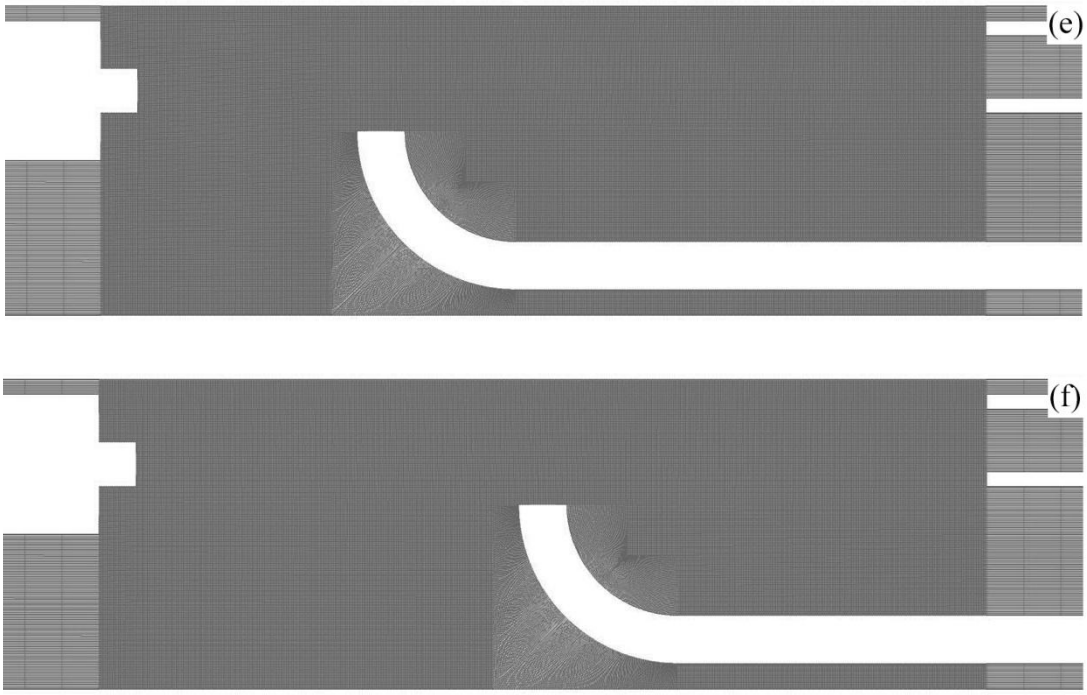

Figure 4.13 (continued)

Table 4.5 Grid quality and grid quantity of model for air Reynolds number of 630

x^*_{pulse}	Grid quality		Grid quantity	
	Minimum Orthogonal	**Maximum Aspect Ratio**	**Cells**	**Nodes**
1	7.07×10^{-1}	52	436,899	440,089
1.67	7.07×10^{-1}	50	437,992	441,162
5	7.07×10^{-1}	50	445,408	448,478
8.33	7.07×10^{-1}	50	452,994	455,963
11	7.07×10^{-1}	50	458,114	461,003
18.33	7.07×10^{-1}	50	472,286	474,956

The synthesis of zinc oxide of these models were predicted using FLUENT® software. The simulated yields of these models are shown in Figure 4.14. The maximum yield of zinc oxide occurred at x^*_{pulse} of 5, at which the maximum entrainment velocity was observed.

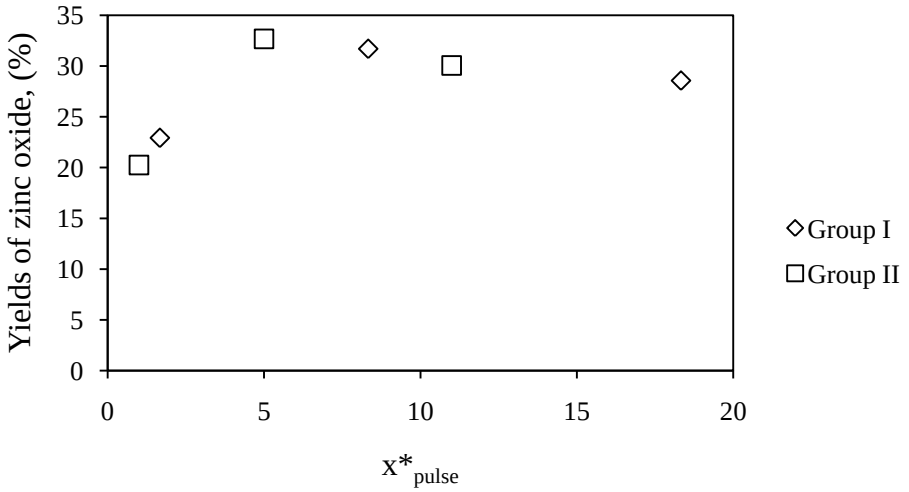

Figure 4.14 Simulated yields of zinc oxide for two different groups (Re_{air} =630)

Simulation results of two different air Reynolds numbers, including 315, and 630, are shown in Table 4.6. These results showed that the maximum yields of zinc oxide occurred at x^*_{pulse} of 8.33 and 5, respectively.

Table 4.6 Summary of zinc oxide yields for two different air Reynolds numbers

x^*_{pulse}	Re_{air} =315		Group I		Group II	
	x*	yield (%)	x*	yield (%)	x*	yield (%)
1	-	-	-	-	0.2	20.24
1.67	0.2	19.53	0.33	22.93	-	-
5	-	-	-	-	1	32.69
8.33	1	31.38	1.67	31.71	-	-
11	-	-	-	-	2.2	30.07
18.33	2.2	28.87	3.67	28.58	-	-

The maximum yields of zinc oxide occurred at x* of 1 because the zinc vapor would be entrained by air jet and reacted with oxygen. The reaction between zinc vapor and oxygen was also dominated by the turbulent mixing due to nitrogen pulse injection. These simulated results were consistent with the experimental work of jet flow. The experimental work [22] revealed that the large-scale coherent structures (CS) in potential core region entrain the environment fluid into the jet shear layers and mixing two fluid (i.e., zinc vapor and oxygen) in smaller-scale.

4.3.2 Effect of pulse characteristic

Effect of pulse characteristic, including pulse injection and continuous injection, on the yield of zinc oxide was studied under the identical total mass of nitrogen. The two different nitrogen inlet velocities are shown in Figure 4.15.

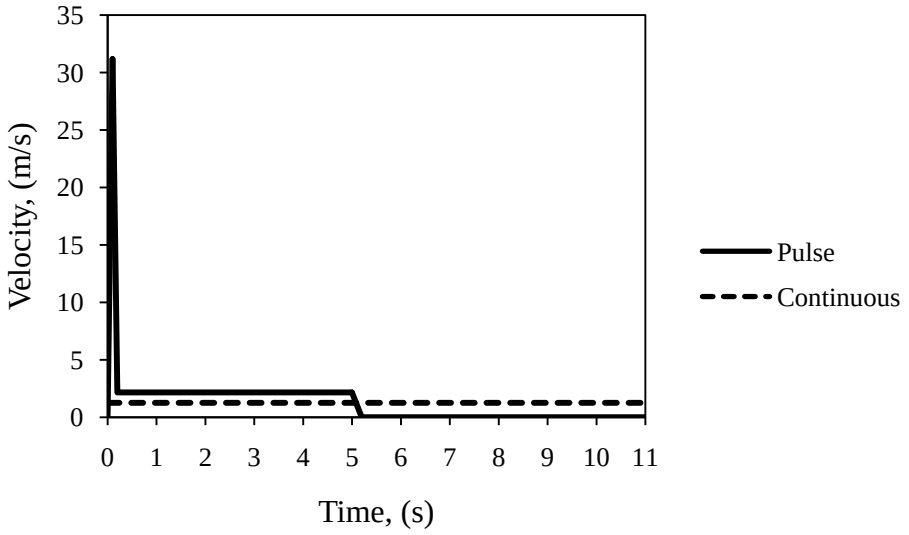

Figure 4.15 Inlet nitrogen velocity for two different pulse characteristics

The effect of pulse characteristic was obtained for different pulse injection position (x^*_{pulse}), including 1.67, 8.33, and 18.33. The contours of velocity, mass fraction of zinc oxide, turbulent kinetic energy, and temperature of the two different pulse characteristics for x^*_{pulse} of 8.33 at t=11.1s and t=19s are shown in Figure 4.16 and Figure 4.17, respectively

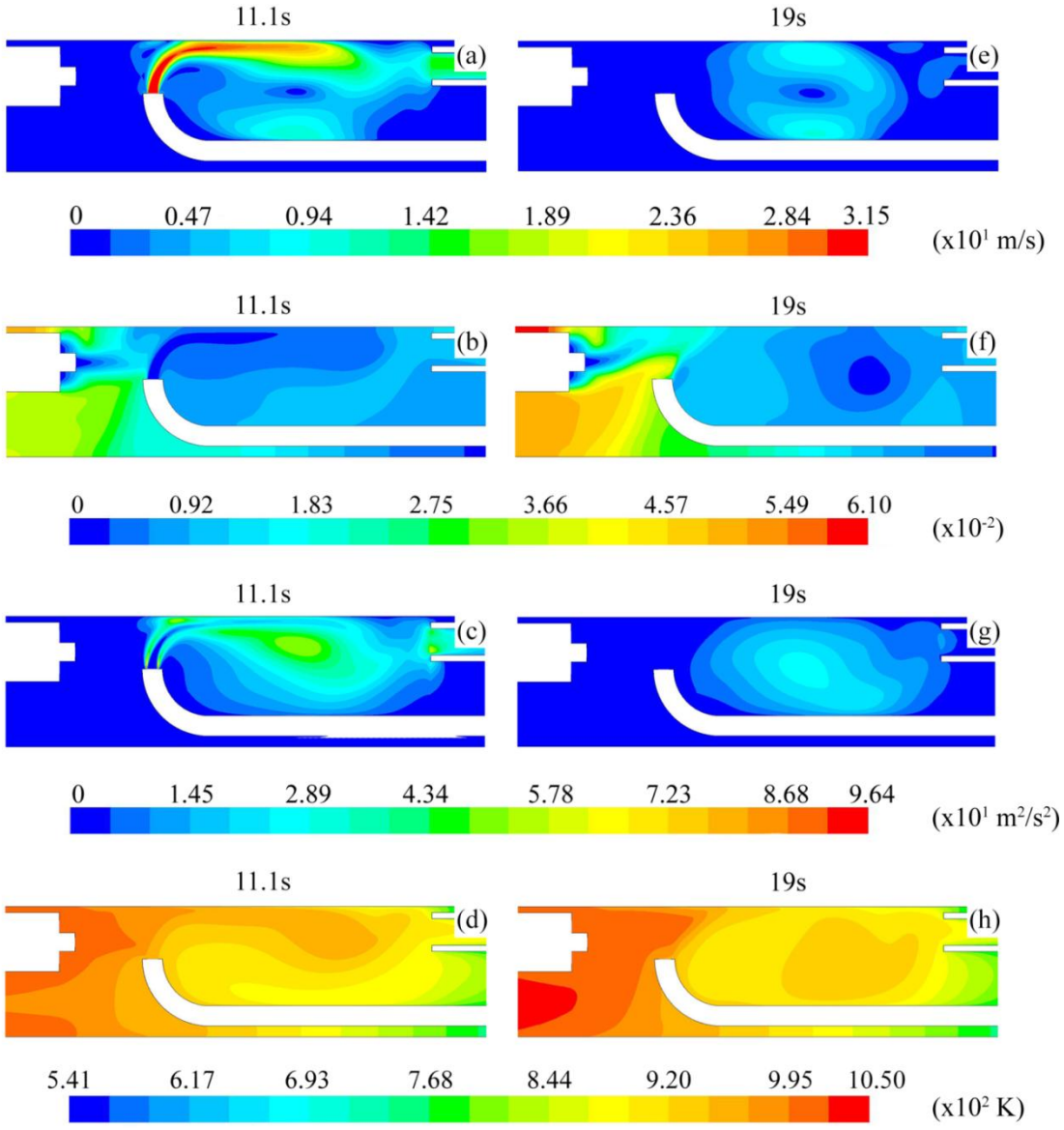

Figure 4.16 The contours of pulse injection with x^*_{pulse} of 8.33 of: (a) velocity, (b) mass fraction of zinc oxide, (c) turbulent kinetic energy, and (d) temperature, at t=11.1s and (e) velocity, (f) mass fraction of zinc oxide, (g) turbulent kinetic energy, and (h) temperature, at t=19s

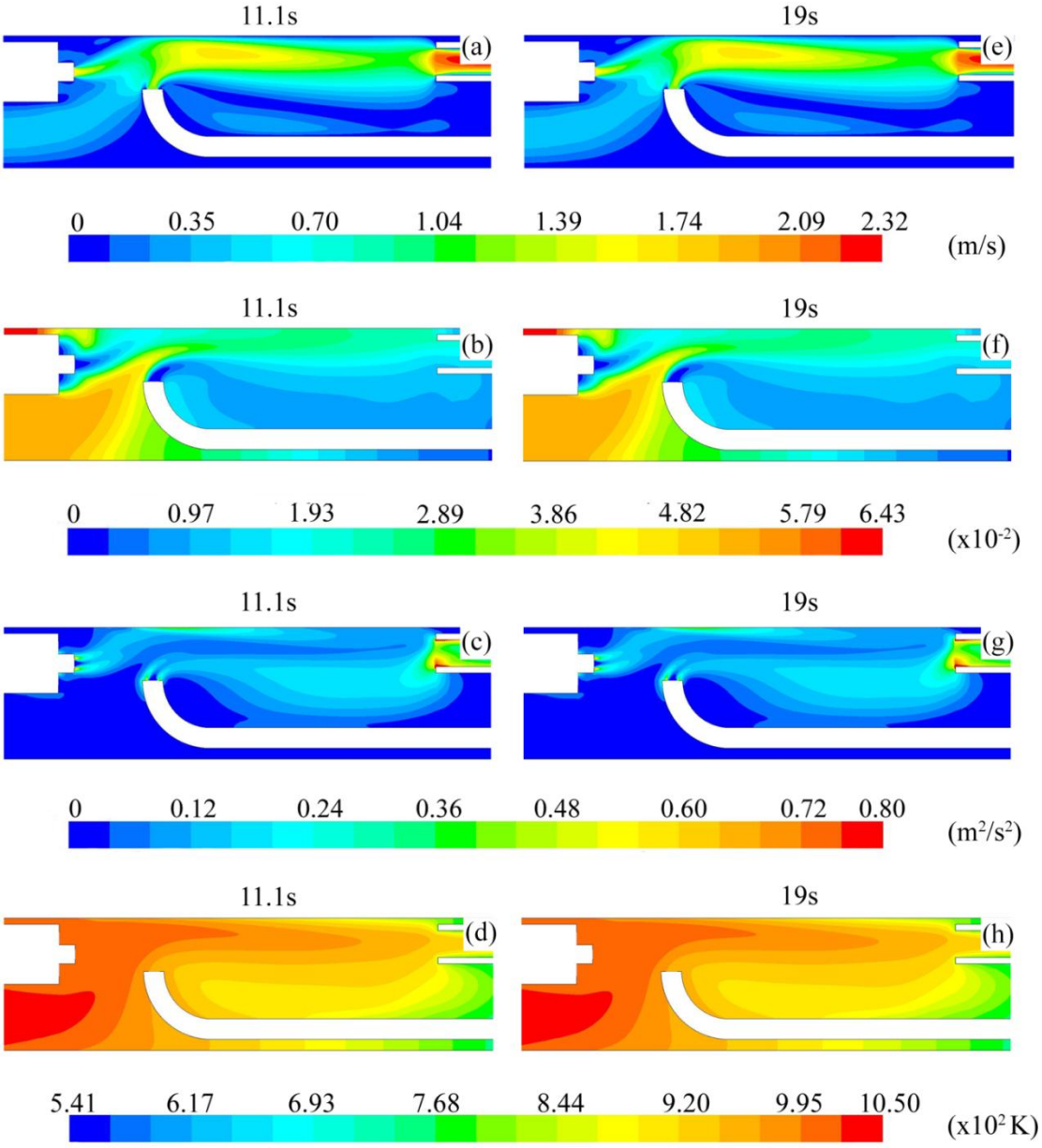

Figure 4.17 The contours of continuous injection with x^*_{pulse} of 8.33 of: (a) velocity, (b) mass fraction of zinc oxide, (c) turbulent kinetic energy, and (d) temperature, at t=11.1s and (e) velocity, (f) mass fraction of zinc oxide, (g) turbulent kinetic energy, and (h) temperature, at t=19s

The calculated yields of zinc oxide of both characteristics for different x^*_{pulse} are shown in Table 4.7.

Table 4.7 Simulated yields of zinc oxide of two different pulse characteristics

x^*_{pulse}	Simulated yields (%)	
	Pulse	**Continuous**
1.67	19.53	29.11
8.33	31.38	38.19
18.33	28.87	37.27

The comparison of zinc oxide yields showed that the yields of continuous injection was greater than the pulse injection for every x^*_{pulse}, i.e. an increase of 49.1%, 21.7%, and 29.1% at x^*_{pulse} of 1.67, 8.33, and 18.33, respectively. The cause of these results would be ascribed by turbulent kinetic energy. Turbulent kinetic energy (k) can be defined as

$$k = \frac{1}{2}\left(\overline{u'^2} + \overline{v'^2} + \overline{w'^2}\right)$$

According to the first assumption of these models, turbulent kinetic energy can be expressed as

$$k = \frac{1}{2}\left(\overline{u'^2} + \overline{v'^2}\right)$$

Turbulent kinetic energy describes the diffusive nature which causes rapid mixing and increased rates of momentum, heat, and mass transfer [16, 17].

The turbulent kinetic energy along longitudinal centerline of air feed tube of two different pulse characteristics are shown in Figure 4.18.

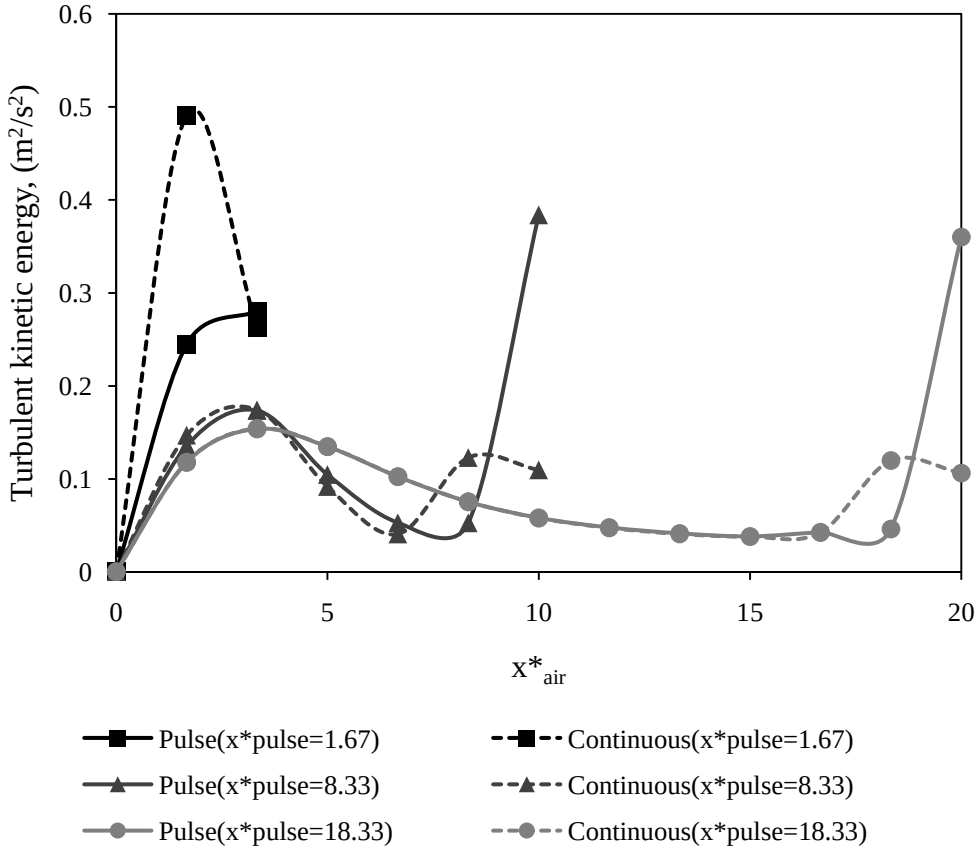

Figure 4.18 Turbulent kinetic energy along air tube centerline of pulse injection and continuous injection with different pulse injection positions

The yields of continuous injection were greater than pulse injection because the turbulent kinetic energy at injection position for continuous injection was greater than pulse injection and injection period time of continuous was longer than another one.

4.3.3 Effect of air feed position

Effect of air feed position, including co-current, and cross current, on the yield of zinc oxide was studied under identical Reynolds number at air feed tube and identical mass of air feed. For the cross current, nitrogen and air were fed at air feed tube and nitrogen pulse tube, respectively.

The effect of air feed position were obtained for different pulse injection position (x^*_{pulse}), including 1.67, 8.33, and 18.33. The contours of velocity, mass fraction of zinc oxide, turbulent kinetic energy, and temperature of two different air feed positions for x^*_{pulse} of 8.33 at t=11.1s and t=19s are shown in Figure 4.17 and Figure 4.19, respectively.

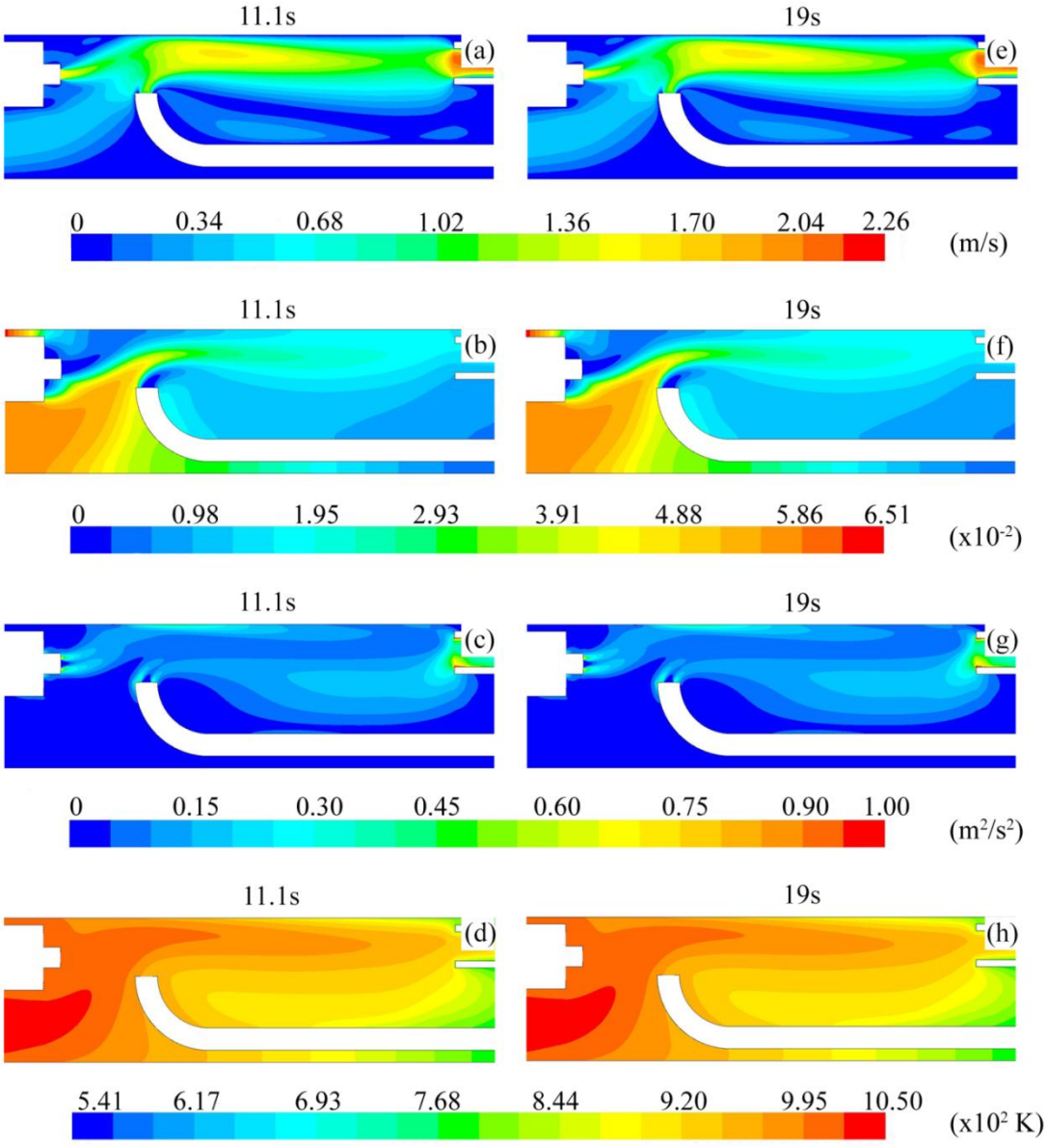

Figure 4.19 The contours of cross current with x^*_{pulse} of 8.33 of: (a) velocity, (b) mass fraction of zinc oxide, (c) turbulent kinetic energy, and (d) temperature, at t=11.1s and (e) velocity, (f) mass fraction of zinc oxide, (g) turbulent kinetic energy, and (h) temperature, at t=19s

The simulated yields of zinc oxide for two different air feed positions with different x^*_{pulse} and the turbulent kinetic energy along longitudinal centerline of air feed tube of two different air feed positions are shown in Table 4.8, and Figure 4.20, respectively.

The simulated yields of zinc oxide showed that the yield of co-current was slightly greater than cross current for every x^*_{pulse}. In addition, the turbulent kinetic energy of co-current was slightly higher than cross current for every x^*_{pulse}. These results revealed that the air feed position was not significant effect on either the yield of zinc oxide or turbulent kinetic energy.

Table 4.8 Simulated yields of zinc oxide of two different air feed positions

x^*_{pulse}	Simulated yields (%)	
	Co-current	**Cross current**
1.67	29.11	28.64
8.33	38.19	38.19
18.33	37.27	36.91

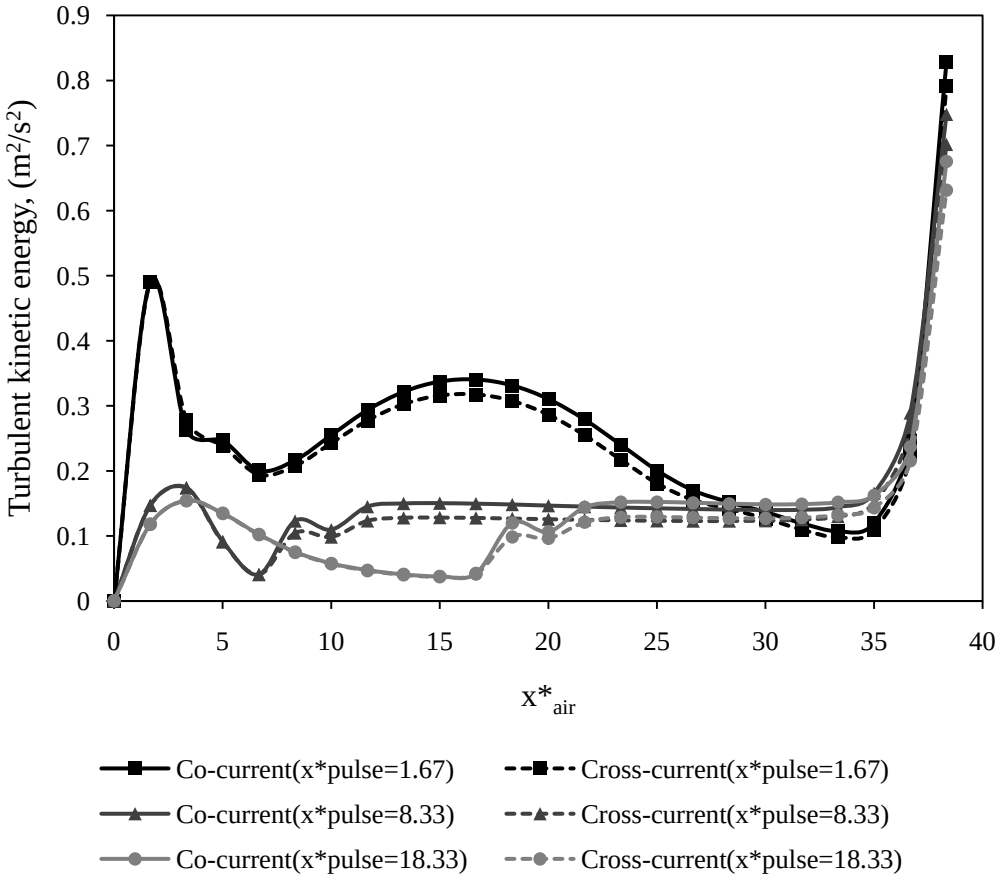

Figure 4.20 Turbulent kinetic energy along air tube centerline of co-current and cross current with different pulse injection positions

CHAPTER V

CONCLUSION AND RECOMMENDATION

5.1 Conclusions

In this work, zinc oxide synthesis by thermal oxidation technique was investigated using a CFD program, FLUENT®. The study focused on the effects of nitrogen pulse injection position and characteristic. In addition, the effects of air feeding position were also investigated. The simulation boundary conditions were set up based on the experimental work of Charnhattakorn et al [14]. The model was simplified to be two dimensional model. Gases were considered to be incompressible and ideal. The fluid motion was considered to be turbulent flow. The homogeneous gas phase reaction was only considered.

The k-epsilon model and species mass transport equations were applied to simulate turbulence and mass fraction of zinc oxide, respectively. Grid generation of all models was generated with grid size of 0.1 mm. The computed yields of zinc oxide were in good agreement with the experimental data [14]. The conclusions of the present research are summarized as follows:

- The pulse injection tube should be placed at the position, which the maximum entrainment velocity was observed, to obtain the maximum yield of zinc oxide. The maximum yield of zinc oxide was due to the turbulent mixing by nitrogen pulse injection and maximum entrainment velocity of jet. These simulated results were in good agreement with the experimental work of jet flow which revealed that the large-scale coherent structures (CS) in potential core region entrain the environment fluid (i.e., zinc vapor) into the jet shear layers and mixing two fluid, (i.e., zinc vapor and oxygen) in smaller-scale.
- The continuous injection characteristic led to greater yields of zinc oxide than the pulse injection. It was due to the higher turbulent kinetic energy at injection position and longer pulse period.

- The yield of zinc oxide and turbulent kinetic energy for co-current flow of air feed were slightly greater than cross current flow. These results revealed that the air feed position was not significant effect on either the yield of zinc oxide or turbulent kinetic energy.

5.2 Recommendation for Future Work

1. Use three dimensional simulation instead of two dimensional simulation to eliminate the error resulting from two dimensional model because turbulence is three dimensional.
2. Use Large Eddy Simulation (LES) instead of k-epsilon turbulence model to simulate large-scale coherent structures (CS) of jet flow.
3. Use PIV method to confirm CFD simulation flow pattern.

REFERENCE

[1] Versteeg, H. K., and Malalasekera, W. An introduction to computational fluid dynamics The finite volume method. Malaysia: Prentice Hall, 1995.

[2] Kaya, F., and Karagoz, I. Numerical investigation of performance characteristics of a cyclone prolonged with a dipleg. Chemical Engineering Journal 151 (2009) : 39-45.

[3] Wanthamanee, S., Bumrungthaichaichan, E., and Wattananusorn, S. Influence of Turbulence promoter Geometry on Flow Pattern in Cross-Flow Membrane Ultrafiltration. Ladkrabang Engineering Journal 29 (2012) : 48-53.

[4] Reuge, N., Bacsa, R., Serp, P., and Caussat, B. Chemical Vapor Synthesis of Zinc Oxide Nanoparticles: Experimental and Preliminary Modeling Studies. Journal of Physical Chemistry C 113 (2009) : 19845-19852.

[5] Nijemeisland, M., and Dixon, A. G. Comparison of CFD simulations to experiment for convective heat transfer in a gas–solid fixed bed**.** Chemical Engineering Journal 82 (2001) : 231-246.

[6] Urgessa, Z. N., Oluwafemi, O. S., and Botha, J. R. Effect of precursor concentration on the growth of zinc oxide nanorod arrays on pre-treated substrates. Physica B 407 (2012) : 1543–1545.

[7] Yu, W., and Pan, C. Low temperature thermal oxidation synthesis of ZnO nanoneedles and the growth mechanism. Materials Chemistry and Physics 115 (2009) : 74–79.

[8] Lim, Y. S., Park, J. W., Hong, S. T., and Kim, J. Carbothermal synthesis of ZnO nanocomb structure. Materials Science and Engineering B 129 (2006) : 100–103.

[9] Shen, L., Zhang, H., and Guo, S. Control on the morphologies of tetrapod ZnO nanocrystals. Materials Chemistry and Physics 114 (2009) : 580–583.

[10] Rosina, M., Ferret, P., Jouneau, P. H., Robin, I. C., Levy, F., Feuillet, G., and Lafossas, M. Morphology and growth mechanism of aligned ZnO nanorods grown by catalyst-free MOCVD. Microelectronics Journal 40 (2009) : 242–245.

[11] Zong, X., and Wang, P. Effect of UV irradiation on the properties of ZnO nanorod arrays prepared by hydrothermal method. Physica E 41 (2009) : 757–761.

[12] Wang, S., Xia, G., Shao, J., and Fan, Z. Structure and UV emission of nanocrystal ZnO films by thermal oxidation of ZnS films. Journal of Alloys and Compounds 424 (2006) : 304–306.

[13] Kim, S., Jeong, M., Oh, B., Lee, W., and Myoung, J. Fabrication of Zn/ZnO nanocables through thermal oxidation of Zn nanowires grown by RF magnetron sputtering. Journal of Crystal Growth 290 (2006) : 485–489.

[14] Charnhattakorn, B., Charinpanitkul, T., Sirisuk, A., and Pavarajarn, V. Controlled synthesis of defects-containing ZnO by the French process modified with pulsed injection and its luminescence properties. Ceramics International 37 (2011) : 2021–2024.

[15] Yamamoto, H., Otani, Y., Seto, T., Nartpochananon, P., and Charinpanitkul, T. Generation of uniform tetrapod-shaped zincoxide nanoparticles by gas-phase reaction with using flow restrictor. Advanced Powder Technology 23 (2012) : 71-79.

[16] OH, H. W. Computational Fluid Dynamics. India: InTech, 2010.

[17] Socolofsky, S. Lecture note on Fluid Dynamics for Ocean and Environmental Engineering. TEXAS A&M UNIVERSITY, 2012.

[18] Bird, R. B., Stewart, W. E., and Lightfoot, E. N. Transport Phenomena. 2nd edition. USA: Wiley, 2007.

[19] ANSYS, Inc. ANSYS FLUENT 12.0 Theory Guide. 2009.

[20] Wilkes, J. O. Fluid Mechanics for Chemical Engineers, 2nd ed., with microfluidics and CFD. 2nd edition. Massachusetts: Prentice Hall, 2006.

[21] Cushman-Roisin, B. ENVIRONMENTAL FLUID MECHANICS. USA: Wiley, 2010.

[22] Wang, X., and Tan, S. K. Environmental fluid dynamics-jet flow. 9th International Conference on Hydrodynamics (ICHD 2010), Shanghai, China, October 11-15, 2010.

[23] Gutmark, E. J., and Grinstein, F. F. FLOW CONTROL WITH NONCIRCULAR JETS[1]. Annual Review of Fluid Mechanics 31 (1999) : 239–272.

[24] Seok, J. K., and Il, W. S. Reynolds number effects on the behavior of a non-buoyant round. Experiments in Fluids 38 (2005) : 801-812.

[25] Yang, J., Sodabanlu, H., Waki, I., Sugiyama, M., Nakano, Y., and Shimogaki, Y. Process design of the pulse injection method for low-temperature metal organic vapor phase epitaxial growth of AlN at 800 ºC. Journal of Crystal Growth 311 (2009) : 383–388.

[26] Zhang, J., Yang, Y., Xu, B., Jiang, F., and Li, J. Shape-controlled synthesis of ZnO nano- and micro-structures. Journal of Crystal Growth 280 (2005) : 509–515.

[27] Hsu, Y. F., Djurisic, A. B., and Tam, K. H. Morphology and optical properties of ZnO nanostructures grown under zinc and oxygen-rich conditions. Journal of Crystal Growth 304 (2007) : 47–52.

[28] Welty, J. R., Wicks, C. E., Wilson, R. E., and Rorrer, G. L. Fundamentals of Momentum, Heat, and Mass Transfer. 5th edition. USA: Wiley, 2008.

[29] Kliem, S., Höhne, T., Rohde, U., and Weiss, F. P. Experiments on slug mixing under natural circulation conditions at the ROCOM test facility using high-resolution measurement techniques and numerical modeling, Nuclear Engineering and Design. 240 (2010) : 2271–2280.

[30] Stern, F., Wilson, R. V., Coleman, H. W., and Paterson, E. G. VERIFICATION AND VALIDATION OF CFD SIMULATIONS. IIHR Report No. 407. Iowa: Iowa Institute of Hydraulic Research, 1999.

APPENDICES

APPENDIX A
C-CODE OF NITROGEN PULSE VELOCITY

```
#include "udf.h"
DEFINE_PROFILE(N2_vel_pulse,thread,index)
{
	face_t f1;
	real t = CURRENT_TIME;
	begin_f_loop(f1,thread)
		{
			real tmod11 = t - (11 * floor(t / 11));
			real y;

			if (tmod11 < 0.1) {
				y = 311.82* tmod11;
			} else if (tmod11 < 0.2) {
				y = (-290.170* tmod11) + 60.199;
			} else if (tmod11 < 5) {
				y = 2.165;
			} else if (tmod11 < 5.2) {
				y = (-10.825* tmod11) + 56.290;
			} else {
				y = 0;
			}
			F_PROFILE(f1,thread,index) = y;
		}
	end_f_loop(f1,thread)
}
```

APPENDIX B
C-CODE OF TEMPERATURE PROFILE

```
#include "udf.h"
DEFINE_PROFILE(temp_wall,thread,position)
{
        real r[3];
        real x;
        face_t f3;
        begin_f_loop(f3,thread)
                {
                F_CENTROID(r,f3,thread);
                x = r[0];
                F_PROFILE(f3,thread,position) = 229049.89*x*x*x*x*x*x*x -
                        401566.64*x*x*x*x*x*x + 255764.26*x*x*x*x*x
                        - 70248.54*x*x*x*x + 2711.18*x*x*x + 2616.07*x + 650.54;
                }
        end_f_loop(f3,thread)
}
```

APPENDIX C
SIMPLE ALGORITHM

SIMPLE stands for Semi Implicit Method for Pressure-linked Equations. This algorithm was introduced by Patankar and Spalding (1972) [1]. This method can be demonstrated by two-dimensional laminar steady flow equations in Cartesian co-ordinates.

$$a_{i,J}u_{i,J} = \sum a_{nb}u_{nb} + \left(p_{I-1,J} - p_{I,J}\right)A_{i,J} + b_{i,J} \quad \text{(C-1)}$$

$$a_{I,j}v_{I,j} = \sum a_{nb}v_{nb} + \left(p_{I,J-1} - p_{I,J}\right)A_{I,j} + b_{I,j} \quad \text{(C-2)}$$

First, the pressure field p^* (guessed pressure) is guessed. Then, substituting p^* into equations (C-1) and (C-2) to yield u^* and v^* as follows

$$a_{i,J}u^*_{i,J} = \sum a_{nb}u^*_{nb} + \left(p^*_{I-1,J} - p^*_{I,J}\right)A_{i,J} + b_{i,J} \quad \text{(C-3)}$$

$$a_{I,j}v^*_{I,j} = \sum a_{nb}v^*_{nb} + \left(p^*_{I,J-1} - p^*_{I,J}\right)A_{I,j} + b_{I,j} \quad \text{(C-4)}$$

Then, the pressure correction and velocities correction can be defined as follows

$$p' = p - p^* \quad \text{(C-5a)}$$

$$u' = u - u^* \quad \text{(C-5b)}$$

$$v' = v - v^* \quad \text{(C-5c)}$$

Subtraction equations (C-3) and (C-4) from equations (C-1) and (C-2), respectively. Then, using correction formulae equations (C-5a)-(C-5c) to yield equations (C-6) and (C-7).

$$a_{i,J}u'_{i,J} = \sum a_{nb}u'_{nb} + \left(p'_{I-1,J} - p'_{I,J}\right)A_{i,J} \quad \text{(C-6)}$$

$$a_{I,j}v'_{I,j} = \sum a_{nb}v'_{nb} + \left(p'_{I,J-1} - p'_{I,J}\right)A_{I,j} \quad \text{(C-7)}$$

Approximating equations (C-6) and (C-7) by eliminate $\sum a_{nb}u'_{nb}$ and $\sum a_{nb}v'_{nb}$. Equations (C-6) and (C-7) become

$$u'_{i,J} = d_{i,J}\left(p'_{I-1,J} - p'_{I,J}\right) \tag{C-8}$$

$$v'_{I,j} = d_{I,j}\left(p'_{I,J-1} - p'_{I,J}\right) \tag{C-9}$$

where $d_{i,J} = \dfrac{A_{i,J}}{a_{i,J}}$ and $d_{I,j} = \dfrac{A_{I,j}}{a_{I,j}}$

Substituting equations (C-8) and (C-9) into equations (C-5b) and (C-5c), respectively. Then, rearranging the results to yield equations (C-10) and (C-11).

$$u_{i,J} = u^{*}_{i,J} + d_{i,J}\left(p'_{I-1,J} - p'_{I,J}\right) \tag{C-10}$$

$$v_{I,j} = v^{*}_{I,j} + d_{I,j}\left(p'_{I,J-1} - p'_{I,J}\right) \tag{C-11}$$

Similar expressions exist for $u_{i+1,J}$ and $v_{I,j+1}$:

$$u_{i+1,J} = u^{*}_{i+1,J} + d_{i+1,J}\left(p'_{I,J} - p'_{I+1,J}\right) \tag{C-12}$$

$$v_{I,j+1} = v^{*}_{I,j+1} + d_{I,j+1}\left(p'_{I,J} - p'_{I,J+1}\right) \tag{C-13}$$

where $d_{i+1,J} = \dfrac{A_{i+1,J}}{a_{i+1,J}}$ and $d_{I,j+1} = \dfrac{A_{I,j+1}}{a_{I,j+1}}$

The velocity field will satisfy continuity equation. The discretised continuity equation is given by

$$\left((\rho uA)_{i+1,J} - (\rho uA)_{i,J}\right) + \left((\rho vA)_{I,j+1} - (\rho vA)_{I,j}\right) = 0 \tag{C-14}$$

Substituting the corrected velocity into equation (C-14) yields the pressure correction equation.

$$a_{I,J}\,p'_{I,J} = a_{I+1,J}\,p'_{I+1,J} + a_{I-1,J}\,p'_{I-1,J} + a_{I,J+1}p'_{I,J+1} + a_{I,J-1}p'_{I,J-1} + b'_{I,J} \tag{C-15}$$

where $a_{I,J} = a_{I+1,J} + a_{I-1,J} + a_{I,J+1} + a_{I,J-1}$ and the coefficients are given in Table C.1.

Table C.1 Coefficients of pressure correction equation and their values

Coefficient	Value
$a_{I+1,J}$	$(\rho dA)_{i+1,J}$
$a_{I-1,J}$	$(\rho dA)_{i,J}$
$a_{I,J+1}$	$(\rho dA)_{I,j+1}$
$a_{i,J-1}$	$(\rho dA)_{I,j}$
$b'_{I,J}$	$(\rho u^* A)_{i,J} - (\rho u^* A)_{i+1,J} + (\rho v^* A)_{I,j} - (\rho v^* A)_{I,j+1}$

The source term b' is the mass imbalance which arising from the incorrect velocity field u^* and v^*. By solving equation (C-15), the correction pressure (p') can be obtained at all points. Then, the correct pressure and correct velocities can be obtained by solving equations (C-5a) and (C-10)-(C-13), respectively.

The earlier approximation does not affect the final solution because the correction pressure and correction velocities will be zero in converged solution giving $p^* = p$, $u^* = u$ and $v^* = v$.

The pressure correction is susceptible to divergence unless some under-relaxation is used during the iterative process and new, improved, pressure p^{new} are obtained with

$$p^{new} = p^* + \alpha_p p' \tag{C-16}$$

where α_p is the pressure under-relaxation factor.

A correct choice of under-relaxation factor (α) is essential for cost-effective simulations. Too large value of α may lead to divergent iterative solutions and a value which is too small will cause extremely slow convergence. Unfortunately, the values of under-relaxation factors are flow dependent and must be sought on a case-by-case basis.

The procedure of SIMPLE algorithm is shown in Figure C.1.

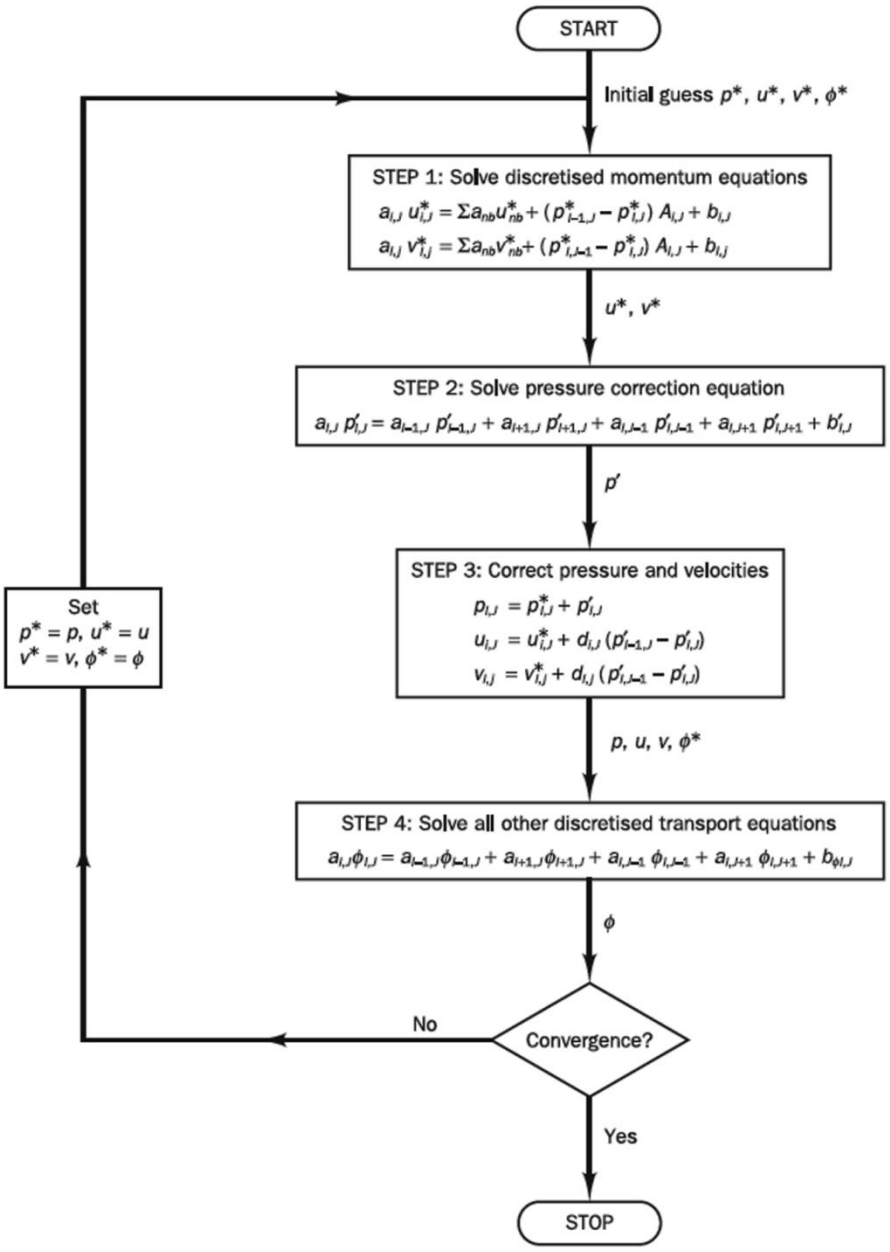

Figure C.1 The SIMPLE algorithm

APPENDIX D
LIST OF PUBLICATIONS

Wanthamanee, S., **Bumrungthaichaichan, E.**, and Wattananusorn, S. Influence of Turbulence promoter Geometry on Flow Pattern in Cross-Flow Membrane Ultrafiltration. Ladkrabang Engineering Journal 29 (2012) : 48-53.

Bumrungthaichaichan, E., Pavarajarn, V., Ponpesh, P., Wattananusorn, S., and Charinpanitkul, T. "CFD simulation of zinc oxide synthesis using pulse injection with thermal oxidation" The 2nd TIChE International Conference 2012 (TIChE 2012), Nakornratchasima, Thailand, October 25-26, 2012.

VITA

Mr. Eakarach Bumrungthaichaichan was born on July 30, 1987, in Nakornratchasima, Thailand. He received a graduated Bachelor Degree of Engineering with the major of Chemical Engineering from King Mongkut's Institute of Technology Ladkrabang. After that, he continued to study in Master degree in Center of Excellence in Particle Technology at Department of Chemical Engineering, Faculty of Engineering, Chulalongkorn University.